UC Berkeley

Title

Mineralogical, magnetic and geochemical data constrain the pathways and extent of weathering of mineralized sedimentary rocks

Permalink

https://escholarship.org/uc/item/9rx7w6vm

Authors

Carrero, Sergio

Slotznick, Sarah P

Fakra, Sirine C

et al.

Publication Date

DOI

Copyright Information

Peer reviewed

1 **Mineralogical, Magnetic and Geochemical Data Constrain the Pathways and Extent of Weathering**

2 **of Mineralized Sedimentary Rocks**

3 *Sergio Carrero[1,2,3], Sarah P. Slotznick[2,4], Sirine C. Fakra[5], M. Cole Sitar[1], Sharon E. Bone[6], Jeffrey L.*

4 *Mauk[7], Andrew H. Manning[7], Nicholas L. Swanson-Hysell[2], Kenneth H Williams[1,8], Jillian F. Banfield[1,2]*

5 *and Benjamin Gilbert[*1,2]*

6 *[1] Energy Geoscience Division, Lawrence Berkeley National Laboratory, Berkeley, CA 94720, USA*

7 *[2] Department of Earth and Planetary Science, University of California, Berkeley, CA 94720, USA*

8 *[3] Institute of Environmental Assessment and Water Research, (IDAEA-CSIC), Jordi Girona 18-26, 08034,*

9 *Barcelona, Spain*

10 *[4] Department of Earth Sciences, Dartmouth College, Hanover, NH 03755 USA*

11 *[5] Advanced Light Source, Lawrence Berkeley National Laboratory, Berkeley, CA 94720, USA*

12 *[6] SLAC National Accelerator Laboratory, Menlo Park, CA 94025, USA*

13 *[7] US Geological Survey, Denver, CO 80225, USA*

14 *[8] Rocky Mountain Biological Lab, Gothic, CO, 81224*

15 *Version to be submitted to GCA*

16

[*]Corresponding author. Tel.: 510-495-2748

E-mail address: bgilbert@lbl.gov (B. Gilbert)

17   **ABSTRACT**

18   The oxidative weathering of sulfidic rock can profoundly impact watersheds through the resulting

19   export of acidity and metals. Weathering leaves a record of mineral transformation, particularly involving

20   minor redox-sensitive phases, that can inform the development of conceptual and quantitative models. In

21   sulfidic sedimentary rocks, however, variations in depositional history, diagenesis and mineralization can

22   change or overprint the distributions of these trace minerals, complicating the interpretation of weathering

23   signatures. Here we show that a combination of bulk mineralogical and geochemical techniques,

24   micrometer-resolution X-ray fluorescence microprobe analysis and rock magnetic measurements, applied

25   to drill core samples and single weathered fractures, can provide data that enable the development of a

26   geochemically consistent weathering model.

27   This work focused on one watershed in the Upper Colorado River Basin sitting within the Mesaverde

28   Formation, a sedimentary sandstone bedrock with disseminated sulfide minerals, including pyrite and

29   sphalerite, that were introduced during diagenesis and subsequent magmatic-hydrothermal mineralization.

30   Combined analytical methods revealed the pathways of iron (Fe), carbonate and silicate mineral

31   weathering and showed how pH controls element retention or release from the actively weathering

32   fractured sandstone. Drill core logging, whole rock X-ray diffraction, and geochemical measurements

33   document the progression from unweathered rock at depth to weathered rock at the surface. X-ray

34   microprobe analyses of a 1 cm size weathering profile along a fracture surface are consistent with the

35   mobilization of Fe(II) and Fe(III) into acidic pore water from the dissolution of primary pyrite, Fe-

36   sphalerite, chlorite, and minor siderite and pyrrhotite. These reaction are followed by the precipitation of

37   secondary minerals such as of goethite and jarosite, a Fe-(oxyhydr)oxide and hydrous Fe(III) sulfate,

38   respectively. Microscale analyses also helped explain the weathering reactions responsible for the

39   mineralogical transformation observed in the top and most weathered section of the drill core. For

40   example, dissolution of feldspar and chlorite neutralizes the acidity generated by Fe and sulfide minerals

41   oxidation, oversaturating the solution in both Fe-oxides. The combination of X-ray spectromicroscopy

42   and magnetic measurements show that the Fe(III) product is goethite, mainly present either as a coatings

43   on fracture surfaces in the actively weathering region of the core or more homogeneously contained

44   within the unconsolidated regolith at the top of the core. Low-temperature magnetic data reveal the

45   presence of ferromagnetic Fe-sulfide pyrrhotite that, although it occurs at trace concentrations, could

46   provide a qualitative proxy for unweathered sulfide minerals because the loss of pyrrhotite is associated

47   with the onset of oxidative weathering. Pyrrhotite loss and goethite formation are detectable through

48   room-temperature magnetic coercivity changes, suggesting that rock magnetic measurements can

49   determine weathering intensity in rock samples at many scales. This work contributes evidence that the

50   weathering of sulfidic sedimentary rocks follows a geochemical pattern in which the abundance of sulfide

51   minerals controls the generation of acidity and dissolved elements, and the pH-dependent mobility of

52   these elements controls their export to the ground- and surface-water.

1. INTRODUCTION

Rock weathering transforms competent bedrock into unconsolidated regolith, initiating soil formation, and releasing elements into groundwater. Weathering proceeds through rock fracturing and a sequence of chemical reactions between rock minerals and water, solutes and atmospheric and subsurface gases. These reactions play an important role in elemental cycles controlling not only element mobility between bedrock and ground or surface water, but also the consumption and potential release of CO_2 depending on the lithology (Kump et al., 2000; Dessert et al., 2003; Hilton and West, 2020) Many factors affect the rates and consequences of rock weathering. Tectonic setting plays a role because high rates of uplift in mountainous regions are associated with high rates of erosion and weathering (Gaillardet et al., 1999; West et al., 2005). Bedrock lithology plays a role with different weathering rates and potential for CO_2 consumption or release for carbonate, shale, or sandstone sedimentary rocks (Meybeck, 1987; Hubbard et al., 2018). The presence of sulfide minerals has a major influence on weathering and watersheds because the oxidative dissolution of sulfide minerals generates acidity that can accelerate mineral dissolution and mobilize metals into freshwater (Gray, 1998; Blodau, 2006; Nordstrom, 2011; Tuttle et al., 2014).

Many watersheds in the Upper Colorado River Basin overlap the Colorado Mineral Belt, which is a northeast-trending, ~500 km-long, 25 to 50-km wide belt of Late Cretaceous to Paleogene plutons and hydrothermal mineral deposits (e.g., Alford et al., 2020; Chapin, 2012; Tweto and Sims, 1963) **(Fig. S1)**. Decadal trends in increasing sulfate concentrations in stream and lake waters reflect climate sensitivity of the weathering of sulfidic rock in some parts of the Rocky Mountains (Mast et al., 2011; Manning et al., 2013), which may increase the release of contaminants such as arsenic (As) (Bondu et al., 2016). Differences in stream chemistry across catchments varying in lithology have illustrated the importance of bedrock composition on acid rock drainage and its impacts on water resources (Verplanck et al., 2009). However, more detailed knowledge of the weathering pathways is necessary for the development of conceptual and quantitative models for weathering sensitivity to temperature and runoff (Manning et al., 2013; Sullivan et al., 2019).

Weathering overprints the host rock with records of mineral reactions, especially reactions involving redox-sensitive phases. These records are generally characterized at the meter scale in more homogeneous lithologies and can be interpreted to generate models for weathering pathways and element export (Brantley and Lebedeva, 2011). In mineralized sedimentary rocks, however, larger-scale weathering patterns can be challenging to identify from bulk observations due to sharp variations in mineralogy and rock chemistry imposed by complex depositional, diagenetic, metamorphic, and mineralization histories. In competent rocks with low permeability, however, weathering mainly occurs around rock fractures, and

86 penetrates a few millimeters into the rock (Gu et al., 2020). At this smaller scale, the bedrock composition

87 is more uniform and hence millimeter-to-centimeter-scale weathering records may provide clearer

88 depictions of the chemical reactions involving in the transformation of unweathered rock (farther from the

89 fracture) to weathered rock (at the fracture). Once these reactions have been well characterized, they may

90 be extrapolated to understand the weathering record throughout the more complex mineralized rock

91 profile.

92   Here we apply meter- and microscale mineralogical and chemical analyses to reveal the sequence of

93 mineralogical transformations and infer the controls on element mobilization and retention within a

94 weathered fracture surface in a hydrothermally altered sandstone from the Redwell Basin, CO.

95 Microfocused X-ray fluorescence spectromicroscopy methods provide the distribution and chemical

96 speciation of major and trace elements in heterogeneous Earth systems (Manceau et al., 2002; Toner et

97 al., 2016) and on mineral changes during weathering reactions (Buss et al., 2008; Bao et al., 2022).

98 Herndon et al. (2014) focused on Mn mobility using micro X-ray fluorescence (µXRF) mapping and

99 micro X-ray adsorption near edge structure (µXANES) spectroscopy to reveal the distribution and

100 speciation of Mn released by shale weathering at the Shale Hills Critical Zone Observatory, PA, USA.

101 Our work expands on these directions with a focus on Fe and sulfide mineralogy.

102   Transformations of Fe-minerals are critical reactions in sulfidic rock weathering but can be

103 challenging to determine by either bulk methods or microchemical studies because the products of sulfide

104 minerals oxidation are typically fine-scale phases at low abundance. Rock magnetic methods can identify

105 Fe-bearing ferromagnetic minerals that are (sub)microscale and at low concentration in rock, and the

106 measurements can be made from sub-centimeter-sized samples. Magnetic methods have been widely

107 applied to soils, paleosols, and sediments to reveal paleoclimate and environmental redox states (Maher

108 and Thompson, 1992; Liu et al., 2012; Slotznick et al., 2018, 2019). There are few studies applying rock

109 magnetic data to constrain the weathering of sulfidic rock (e.g., Chevrier et al., 2006; Essalhi et al., 2011).

110 In this study, we integrate whole rock geochemical data with microfocused X-ray fluorescence

111 spectromicroscopy, magnetic methods, and scanning electron microscopy (SEM) data to develop a

112 conceptual model of the key geochemical and mineralogical transformations associated with weathering

113 and element release pathways throughout the Redwell Basin.

2. MATERIALS AND METHODS

2.1. Site description

116   Redwell Basin, in south-central Colorado, USA, is a small alpine hanging glacial valley located in the

117 Upper Colorado River Basin at an elevation of ~3300 m (**Fig. 1**). The bedrock of the basin is a thick

118 transitional package of late Cretaceous marine mixed shales (Mancos Shale) to marginal marine mixed

119 sandstone and shale (Mesaverde Formation) (Gaskill et al., 1967). The basin was intruded 15.767 ± 0.028

120 million years ago by a porphyritic granite stock that hosts the Mt. Emmons porphyry Mo deposit (Thomas

121 and Galey, 1982; Rosera et al., 2021). The associated hydrothermal activity formed a near-surface

122 stockwork deposit consisting of veins filled by quartz, feldspar and sulfide minerals (Sharp, 1978). The

123 Daisy Mine and other small workings in Redwell Basin exploited polymetallic veins; these mines are now

124 inactive (**Fig. 1**).

125   The Redwell Basin drains to the Redwell Creek, a tributary of the Gunnison River, which is an

126 important source of drinking and irrigation water in the area. In the highest-altitude reach of Redwell

127 Creek, the water pH is circumneutral, but downstream inputs of surface and subsurface waters affected by

128 the oxidative weathering of sulfide minerals lower the pH to below 4 and increase the concentration of Zn

129 and other metals (Verplanck et al., 2004; Kimball et al., 2010). Mixing analysis indicates that ~3/4 of the

130 Zn and ~1/2 of the dissolved sulfate originate from mining-related activities that exposed sulfidic rock to

131 oxygenated fluids (Wanty et al., 2004).

132   A 50 m core (MW1) was drilled in 2017 at 3404 m elevation (**Fig. 1 and S2**), above the start of

133 perennial flow in Redwell Creek, higher than mining activities near the Daisy Mine. This core is stored in

134 the USGS Core Research Center in Lakewood, CO.

135 **2.2. Rock Sampling and Sample Preparation**

136   Samples were collected from the MW1 core at approximately 0.5 m intervals between the upper part

137 of the core and 13 m below ground surface (bgs), and every 3 meters between 13 m and 45 m bgs, to

138 obtain chemical and mineralogical depth profiles. All samples were collected from core with moderate to

139 low concentrations of hydrothermal mineralization; veins filled by sulfide minerals and areas with high

140 visible concentrations of disseminated sulfide minerals were avoided. A second group of samples were

141 collected from the first 10 meters of core where weathering could be identified around fractures on the

142 rock by changes in color or texture (**Fig. S2**). The weathering profiles were revealed by cuts perpendicular

143 to the fracture surfaces and were made into thin sections for microfocused X-ray spectromicroscopy and

144 optical and electron microscopy. In addition, several 2-mm-thick slices were cut parallel to the fracture

145 surface for rock magnetic analysis of layers representing weathered (fracture surface) and unweathered

146 zones.

147 **2.3. Analytical Techniques**

148 *2.3.1. Elemental analyses*

149   Bulk samples were analyzed for major and trace elements quantification in the laboratory of ALS

150 Global (Reno, NV). Major components (SiO_2, Fe_2O_3, Al_2O_3, CaO, MgO, Na_2O, K_2O, Cr_2O_3, TiO_2, MnO,

151 P_2O_5, SrO and BaO) were analyzed following the method ME-IPC06, whereas trace elements were

152 analyzed by methods ME-MS81 (Ba, Ce, Cr, Cs, Dy, Er, Ga, Gd, La, Sn, Sr, U, V, W, Y, Yb, Zr), ME-

153 MS42 (As, Hg, Sb, Se) and ME-4ACD81 (Ag, Cd, Co, Cu, Ni, Pb, Sc, Zn). In all these methods, rock

154 samples were melted in lithium borate and digested in aqua regia, following an Inductively Coupled

155 Plasma Atomic Emission Spectroscopy (ICP-AES) analysis, for ME-IPC06 and ME-4ACD81, or

156 Inductively Coupled Plasma Mass Spectroscopy (ICP-MS), for ME-MS42 and ME-MS81. Carbon and S

157 were analyzed by combustion and infrared detection according to the methods C-IR07 and S-IR08,

158 respectively. We assume that the C is inorganic C because the drill core is typically light green to light

159 gray sandstone and contains no visible organic material. Mass balance constraints indicate that all C in

160 78% of the samples could be accounted for by Ca-Mg-Mn carbonate minerals, and the remaining 22%

161 may contain 0.04 to 0.35 weight percent organic C. Detection limits were 0.01% in weight for major

162 elements (Al, C, Ca, Cr, Fe, K, Mg, Na, P, S, Si, Sr, Ti) and 10 ppb for As, Cr and Cu; 1 ppb for Cd; 100

163 ppb for Mn, Se and Zn; 40 ppb for Ni; and 5 ppb for Pb; with an analytical error lower than 5%. The mass

164 transfer coefficient (τ) was calculated to assess the elemental profile and the relative change in

165 concentration due to changes in other elements in the rock, according to the following equation (Brimhall

166 and Dietrich, 1987; Anderson et al., 2002):

167 $$\tau_{i,j} = \frac{C_{j,w}\, C_{i,p}}{C_{j,p} C_{i,w}} - 1 \qquad\qquad (1)$$

168 where $C_{j,w}$ and $C_{j,p}$ indicate the concentration of the element j in the weathered and parent samples,

169 respectively, and $C_{i,w}$ and $C_{i,p}$ are the concentration of the immobile element (Zr in this case) in the

170 weathered and parent sample, respectively. Positive $\tau_{i,j}$ values indicate enrichment of the element j, and

171 negative values indicate depletion with respect to the parent (in our case sample at 12.1 m bgs). The

172 parent reference sample was chosen based on no weathering reactions noted in hand sample observation

173 and low or no mineralization according to Zr concentration (< 400 ppm, natural break in the core between

174 mineralized and not mineralized samples). The sample at 12.1 m bgs achieves these requirements and also

175 displays relatively immobile elemental concentrations close to median value of the population (e.g.,

176 element, median, sample: SiO_2 % 70.7 vs 70,7; TiO_2 % 0.5 vs 0.48; or Zr ppm 228 vs 300).

177 *2.3.2. X-ray diffraction*

178   *2.3.2.1. Clay mineral Analysis*

179   The clay fraction was extracted from bulk samples to assess the clay mineral composition and

180 abundance, following the protocol described by Moore and Reynolds (1997). The principal steps are: (1)

181 placing 10 g of ground rock into 40-mL polycarbonate centrifuge tubes and adding Milli-Q water at a

182 solid to liquid ratio of 1:10 (by weight), (2) sonicating in three cycles of 30 min for cement dissolution

183 and clay mineral desegregation, (3) leaching with oxalic acid (0.1 M) for Fe-oxide dissolution; (3)

184 addition of sodium pyrophosphate (1 mM) as a clay mineral dispersive agent and sonicating again; (5)

185 decantation to remove particles greater than 2 µm, waiting 4 hours and carefully removing the first 5 cm
186 where all suspended particles are < 2 µm. To quantify the total clay mineral proportion, step 5 was
187 repeated as many times as needed until the first 5 cm of supernatant were totally clear of suspended
188 particles. The remnant non-clay fraction was washed in Milli-Q water several times, dried at room
189 temperature and weighed. The mass of the clay fraction was calculated from the difference in weight
190 between steps 1 and 5.

191   *2.3.2.2. Data acquisition*
192   The mineralogical composition of rock samples were analyzed using XRD (Chung, 1974) on a
193 Rigaku SmartLab high-resolution XRD diffractometer using Bragg-Brentano geometry. The
194 diffractometer was equipped with a theta-theta goniometer and a rotating sample holder using Cu ($\lambda k\alpha 1 =$
195 1.5406 Å and $\lambda k\alpha 2 = 1.5444$ Å) cathode. For clay mineral identification, an aliquot from the < 2 µm
196 particle size suspension was dropped on a zero-background plate and dried at room temperature to obtain
197 oriented clay mineral samples. Bulk rock was ground, obtaining a fine homogeneous powder, and placed
198 in an aluminum holder to ensure random particle orientations. Bulk rock samples were collected from 2 to
199 90 °2θ with a 0.02 °2θ step-size and count times of 2 seconds per step. Oriented clay mineral samples
200 were measured (3 to 25 and 3 to 75 °2θ with 0.02 °2θ step-size and 10 and 2 seconds per step,
201 respectively) under four different conditions: (1) dry at room temperature, (2) saturated with ethylene-
202 glycol for 1 hour at 333 °K, (3) heated at 673 °K for 1 hour, and (4) heated at 823 °K for 1 hour. The
203 diffraction patterns were analyzed using the software Match! (Putz and Brandenburg, 2011) and the PDF-
204 2 mineral database (Gaste-Rector and Blanton, 2019).

205 *2.3.3. Scanning electron microscopy*
206   A scanning electron microscopy (SEM) instrument (Zeiss Evo LS10) equipped with an energy-
207 dispersive X-ray spectroscopy (EDX) detector was used to analyze gold-coated rock thin sections. Back-
208 scatter electron (BSE) imaging with the SEM was performed using a 5.0 kV accelerating voltage and 1.5
209 µm spot size. EDX was performed at 30 kV using a 3.0 µm spot size. Semi-quantitative chemical
210 analyses by EDX provide an approximate stoichiometric composition, allowing mineral identification.

211 *2.3.4. Synchrotron X-ray spectromicroscopy.*
212   µXRF imaging and µXANES spectroscopy were performed on XFM beamline 10.3.2 at the
213 Advanced Light Source (ALS, Berkeley, CA, USA, Marcus et al., 2004) for tender- and hard-X-ray
214 analysis and on beamline 2-3 at the Stanford Synchrotron Radiation Light Source (SSRL, USA) for hard-
215 X-ray analysis.
216   At ALS beamline 10.3.2, µXRF mapping and µXANES were performed under ambient conditions.
217 All data were recorded with a single element silicon drift fluorescence detector (Amptek FAST XR-

218 100SDD). µXRF elemental maps (S, P, Si, Al) were collected at 2700 eV (~230 eV above the S K-edge)

219 using 20 × 20 µm pixel size and a beam spot size of 4 × 4 µm. µXRF spectra were simultaneously

220 collected on each pixel of the maps. All maps were then deadtime-corrected, and decontaminated using

221 custom LabVIEW 2018 (National Instruments, Austin, TX, USA) software available at the beamline

222 (xraysweb.lbl.gov/uxas/Databases/Overview.htm). Elemental maps were then analyzed with a

223 MatlabR2020b routine available at beamline 10.3.2. µXRF spectra were recorded at 10 keV at specific

224 locations on the maps. Sulfur K-edge µXANES spectra were recorded areas with high S concentration

225 and low or high correlation with other elements, according to statistical PCA analysis. Spectra were

226 recorded by continuously scanning the Si (111) monochromator (Quick XAS mode) in the 2450 to 2550

227 eV range, with 0.2 eV steps around the edge. These spectra were then background-subtracted using a

228 spectrum recorded in air (sample out). Spectra were subsequently deadtime corrected, deglitched,

229 calibrated, pre-edge background subtracted and post-edge normalized using custom LabVIEW 2018

230 software available at 10.3.2. Spectra were calibrated using gypsum ($CaSO_4$), with its main peak (white

231 line) set at 2482.75 eV. Sulfur K-edge µXANES of mineral standards (jarosite and sphalerite) were

232 obtained from the S XANES mineral database of the European Synchrotron Radiation Facility ID21

233 beamline.

234   µXRF images were also collected at SSRL at beamline 2-3 using a Si(111) double crystal

235 monochromator. The fluorescence signal was monitored with a Vortex Silicon Drift Detector. Samples

236 were monitored at room temperature in air. In this experiment, the weathering profile maps were collected

237 at 13000 eV and 5 × 5 µm pixel size Se. Iron chemical maps were carried out with a 10 × 10 µm pixel

238 size at six different energies (7114.9, 7121, 7126.2, 7126.4, 7137.1 and 7210 eV). An approximate

239 distribution map for Fe(II) was generated in the SMAK software (Webb, 2011) by subtracting the

240 background intensity at 7114.9 eV from the intensity at 7126.2 eV, which is dominated by Fe(II) in

241 various minerals. An approximate distribution map for Fe(III) was generated by subtracting the Fe(II)

242 distribution from total Fe (map at 7210 eV). Elemental profiles for Mn, Fe, Ca and K were obtained from

243 the map collected at 7210 eV (~100 eV above the Fe K-edge). Due to limited beamtime, a map right

244 above the Mn K-edge and below the Fe K-edge was not recorded, therefore the Mn map can still have

245 residual signal from Fe because of high Fe content. The elemental profile for Zn was obtained from a map

246 collected at 10keV in the same region.

247   Iron K-edge µXANES spectra collected at SSRL were recalibrated according to the ALS XFM10.3.2

248 convention, using an Fe foil with first inflection point set at 7110.75 eV (Kraft et al., 1996). The spectra

249 were analyzed with Athena software, IFFEFIT package 0.9.26 (Ravel and Newville, 2005). Least-squares

250 linear combination fitting (LCF) of Fe K-edge µXANES data was subsequently carried using custom

251 LabVIEW 2018 software available at beamline 10.3.2, following the procedures described elsewhere

252 (Heller et al., 2017). LCF fits were performed in the range 7090 to 7365 eV, using the large Fe XAS

253 database of XFM beamline 10.3.2 to confirm the oxidation state of Fe and further identify the major

254 mineral groups present. The best fit, using a maximum of three components, was chosen based on the

255 minimum normalized sum-square value (NSS $=100\times[\sum(\mu_{exp}-\mu_{fit})^2/\sum(\mu_{exp})^2]$), for which the addition of a

256 spectral component to the fit required a 10 % or greater improvement in the NSS value.

2.4. Rock magnetic analyses

258 Rock magnetic experiments were performed to detect and characterize ferromagnetic minerals, a term

259 used broadly (in latin, *sensu lato*), to encompass minerals that have high magnetic susceptibility and can

260 retain a remanent magnetization, but have a broad range of magnetic ordering behavior. The analyses

261 were performed on bulk samples as well as samples of thin rock layers from three weathering profiles.

262 At the Institute for Rock Magnetism at the University of Minnesota, hysteresis loops and direct

263 current demagnetization measurements were performed at room temperature using a Princeton

264 Measurements Vibrating Sample Magnetometer (VSM). Seven samples (four from the weathering profile

265 and three below it) were also subject to low-temperature experiments to further constrain the

266 identification of ferromagnetic minerals. Using a Quantum Designs Magnetic Property Measurement

267 System, samples were: (1) cooled in a 2.5 Tesla (T) field from 300 to 10 K, then the field was turned off,

268 and remanence measurements were made upon warming (field-cooled low-temperature saturation

269 isothermal remanent magnetization, FC LTSIRM); (2) cooled again to 10 K with no applied field, at

270 10 K pulsed with a 2.5 T field, and then remanence measurements were made upon warming (zero-field-

271 cooled low-temperature saturation isothermal remanent magnetization, ZFC LTSIRM); (3) pulsed with a

272 2.5 T field at 300 K before cooling to 10 K and warming back to 300 K during which remanence

273 measurements were collected (room temperature saturation isothermal remanent magnetization,

274 RTSIRM).

275 These low-temperature experiments probe different aspects of temperature-dependent magnetic

276 behavior. Sharp drops or increases in magnetization during warming and cooling cycles are related to

277 well-characterized magnetic and/or crystallographic phase transformations of ferromagnetic minerals.

278 RTSIRM curves can capture these transitions and their reversibility (or lack thereof) which gives insights

279 into mineralogy and grain size. In addition to probing for these characteristic transitions, LTSIRM

280 experiments compare warming curves where a sample was cooled under a strong field (FC) or not (ZFC)

281 and can be used to identify additional minerals as some ferromagnetic minerals will differentially acquire

282 magnetization under these conditions.

283 All samples were additionally analyzed at the UC Berkeley paleomagnetism lab using a 2G

284 Enterprises superconducting rock magnetometer (SRM) with RAPID automatic sample handling and

285 software (Kirschvink et al., 2008). Isothermal remanent magnetization (IRM) acquisition and alternating

286 field demagnetization experiments were conducted to develop coercivity spectra with lower noise than on

287 the VSM. Coercivity is an inherent property of ferromagnetic minerals related to how easily they are

288 demagnetized (e.g., Peter and Dekkers, 2003), and coercivity spectra of specimens with complex mineral

289 assemblages can be used to identify different mineral phases through peak fitting software; MaxUnMix

290 was utilized here (Maxbauer et al., 2016). Several of the samples including those from the main fracture

291 were additionally analyzed for rotational remanent magnetization (RRM) acquisition and demagnetization

292 and anhysteretic remanent magnetization acquisition and demagnetization (before higher-field analyses at

293 the University of Minnesota); data were processed using the RAPID Matlab codes (Kirschvink et al.,

294 2008). The presence of RRM can be used to identify magnetic Fe-sulfide phases like pyrrhotite, although

295 the sensitivity limits are not well understood (Thomson, 1990; Snowball, 1997).

296 # 3. RESULTS

297 ## 3.1. Bulk Measurements of Core Lithology and Weathering

298 The Redwell Basin core MW1, shown in **Figures 2a** and **S2**, displays a hydrothermally altered and

299 locally fractured sedimentary sequence composed of competent fine-grained sandstone interstratified with

300 shale and siltstone (Thomas and Galey, 1982) (**Fig. S3**). Hydrothermal alteration led to the formation of

301 polymetallic veins up to ~3-cm thick composed of quartz and sulfide minerals, increasing the

302 heterogeneity of the sedimentary mineral association.

303 The topmost section of the core, from 2 to 2.8 m bgs, is unconsolidated and visibly weathered, with

304 an ochre color. The depth of 2.8 m bgs marks an abrupt transition to more competent sandstone that

305 contains varying fracture density and orientation with depth. Between 2.8 and 10.7 m bgs a number of the

306 fractures (approximately 10 out of 40) show evidence of weathering on the fracture surfaces. Beneath this

307 depth, the fracture surfaces are unweathered. Manning et al. (2020) reported mineralogical, geological

308 and groundwater geochemical data from the same core and borehole, MW1. The Mesaverde Formation at

309 this location displays subhorizontal bedding-plane parallel fractures, and steeply dipping fractures

310 (**Fig.S3**). The permeability is dominantly controlled by subhorizontal fractures, and currently active

311 groundwater flow occurs close to the water table, the top of which fluctuates from approximately 8.8 m

312 bgs down to a depth of 20 m bgs. Groundwater has an average pH of 5.5 at the water table position,

313 increasing to 7.5 at the bottom of the drill hole (Manning et al., 2020).

314 *3.1.1. X-ray Diffraction and Elemental Composition*

315 Bulk rock XRD and XRD analyses of clay minerals separates reveal variations in mineralogy

316 throughout the core (**Fig 2a**). The uppermost weathered sample (2 m bgs) is dominated by quartz (35 %)

317 and phyllosilicate minerals (62 %) that bulk and clay mineral analysis as chlorite, illite, muscovite and

318 kaolinite (**Fig. S4**), with complete loss of plagioclase and orthoclase. Below this position, the core is

319   composed by 40 to 60 % of quartz, 10 to 25% of feldspar (mostly albite and orthoclase), 10 to 40%

320   chlorite and micas (illite and muscovite). The clay mineral and mica fractions reach 60% in some shale

321   levels. Clay mineral analysis also identify vermiculite in the samples located above 5 m bgs (**Fig. S4**), the

322   bulk XRD data cannot quantify its abundance. Accessory jarosite is detected by XRD only in one sample

323   at 2 m bgs, whereas pyrite is detected at several depths (e.g., 3.3, 5.7 and 11.9 m bgs). However, paired

324   SEM-EDX observations and magnetic analyses (detailed below) identify additional accessory minerals

325   including pyrrhotite, magnetite, sphalerite, galena, several metal-oxides, calcite, and siderite.

326   Whole rock geochemistry shows depletion of S, Ca, and Zn above 3.3 m bgs with concomitant

327   enrichment of Fe (**Fig. 2b, Table S1 and S2**). Below this, the S concentrations displays strong variations

328   with depth where samples that are enriched in S are also enriched in Zn, Ni, Mn, and/or Fe, especially at

329   3.9, 5.7, and 11.9 m bgs (**Fig. 2b**). Major elements such as Ca and K show highly variable concentrations,

330   and their enrichments do not necessarily coincide with S and metal enrichments. Selenium has low

331   concentrations throughout the core, but samples with relative Se enrichments are also relatively enriched

332   in S. Finally, the C concentrations (**Table S1**) indicate that upper areas (above 3 m bgs) highly affected by

333   weathering reactions contain much lower concentrations of carbonate minerals whereas less weathered

334   samples display a variable concentration in carbonate minerals.

335   *3.1.2. Rock Magnetic Analyses*

336   Additional insights into Fe and S mineralogy in selected samples were obtained using non-

337   destructive bulk magnetic techniques. These methods are very sensitive to ferromagnetic minerals, such

338   as pyrrhotite, magnetite and siderite, but cannot detect non-ferromagnetic minerals such as pyrite or

339   sphalerite. As a consequence, magnetic measurements do not provide complete mineralogical phase

340   analysis. Nonetheless, most ferromagnetic minerals are reactive during weathering and thus may provide

341   a proxy for weathering intensity even where present in low abundance.

342   *3.1.2.1. Low-Temperature Magnetic Measurements*

343   Low-temperature magnetic techniques reveal complex assemblages of ferromagnetic minerals (**Fig.**

344   **3**). Hematite and magnetite are identified in the samples based on their characteristic low-temperature

345   magnetic transitions: the Morin transition at ~250 °K (hematite) and the Verwey transition at 120 °K

346   (magnetite) (Verwey, 1939; Morin, 1950). Some of the magnetite may be partially oxidized to

347   maghemite, even in unweathered samples, based on the slight humped shape of the RTSIRM curves

348   (Ozdemir and Dunlop, 2010). Monoclinic pyrrhotite is identified by the non-reversible Besnus transition

349   at 32 °K (Besnus and Meyer, 1964; Rochette et al., 1990) in all but one of the unweathered sandstone

350   samples. Siderite becomes antiferromagnetic at low temperatures and can be identified in magnetic

351   experiments due to its reversible magnetic transition at its Néel temperature of 37 °K and characteristic

behavior of the FC LTSIRM values being much greater than those in the ZFC LTSIRM experiment (Frederich et al., 2003). The Fe carbonate siderite is detected in all but the deepest of the unweathered samples. Due to similar transition temperatures, siderite identification is tentative in samples that contain both pyrrhotite and siderite and relied on qualitative comparison of the FC and ZFC LTSIRM experimental data.

3.1.2.2. Room-Temperature Magnetic Measurements

Room-temperature measurements of coercivity spectra can provide additional information on the ferromagnetic mineral content of a larger number of samples (**Fig. 3b**). The DC demagnetization data are noisy, due to the small sample-size and low abundance of ferromagnetic phases, making the IRM demagnetization analyses dependent on the more sensitive SRM for interpretation (even though the applied field values are lower) (**Fig. S5**). Due to overlapping coercivity ranges for different minerals (Peter and Dekkers, 2003), unique mineral identification even in numerically unmixed spectra is difficult. Nevertheless, with reference to the low-temperature experimental results, a moderate coercivity component (12 to 31 mT, rage from samples unmixed spectra) is tentatively linked with magnetite, a high moderate coercivity (41 to 111 mT) is interpreted as pyrrhotite, and a high-coercivity component (139 to 527 mT) is suggested to be hematite and/or goethite. A low coercivity component (5 to 7 mT) is difficult to interpret; it could be magnetite of a distinct grainsize (very-fine or very coarse) (Dunlop, 1986; Egli, 2004), titanomagnetite, a poorly characterized compositionally mixed sulfide minerals (Kim et al., 2000; Slotznick et al., 2019), or even very coarse ferrihydrite (Pannalal et al., 2005; Berquo et al., 2007).

The saturation magnetization at room temperature varies by over a factor of 100 across the 15 unweathered samples (note the log-scales in **Fig. 3a** and right plot in **Fig. 3b**). Saturation magnetization roughly correlates to the abundance of ferromagnetic minerals (especially pyrrhotite and magnetite) highlighting differences in the original unweathered bedrock.

The dominant feature in the sample coercivity data is an interval from ~3.7 to 6.7 m bgs that is enriched in ferromagnetic minerals inferred to be magnetite and pyrrhotite; these samples also show moderately high saturation magnetization values (**Fig. 3b**). This depth range includes one of the samples with detectable pyrite in XRD and an enrichment of Zn that reflects sphalerite in quartz veins, and thus represents a zone of higher hydrothermal fluid flow and mineralization associated with the porphyry intrusion. The uppermost two samples (2 m and 2.6 m bgs) contain only goethite/hematite and the moderate-coercivity component. One sample at ~18.3 m bgs exhibits more than an order of magnitude increase in magnetization as well as the largest proportion low-coercivity component and the lowest paramagnetic to ferromagnetic ratio.

3.2. Microchemical Analyses of Fracture-Scale Weathering

385   To elucidate the weathering processes distinct from the stratigraphic variations of hydrothermal

386   alteration intensity, samples were prepared from a visibly weathered fracture surface at a depth of 3.3 m

387   bgs (**Fig. 4a**). Sections cut normal to the fracture surface show evidence of weathering reactions, with an

388   ochreous coating on mineral grains proceeding into the rock from the fracture surface (**Fig. 4b and S6**).

389   The clay mineral content of the topmost layer, noticeable as fine-grained minerals in optical microscopy

390   (**Fig. S6**), indicate that the fracture opened in a shale layer within the sandstone.

391   *3.2.1. SEM-EDX Analysis*

392   Two-dimensional imaging and elemental analysis using SEM–EDX on a polished thin section from

393   the drill core shown in **Fig. 4** confirmed the major mineralogy of the unweathered rock away from the

394   fracture; made of quartz, plagioclase, orthoclase and chlorite. The SEM-EDX data show evidence of

395   plagioclase and orthoclase replacement by sericite, which is fine-grained white mica that is a common and

396   abundant hydrothermal alteration mineral in the phyllic and propylitic alteration zones of magmatic-

397   hydrothermal ore deposits (**Fig. 4c-III**; Seedorff et al., 2005; Thomas and Galey, 1982). The SEM and

398   XRD also identify Fe-rich chlorite and kaolinite (**Fig. 4c-VII, S7 and S8**). SEM analysis of the least

399   weathered part of this sample documents the presence of accessory minerals such as sphalerite that may

400   contain up to 10% Fe, minor galena that occurs locally as inclusions in sphalerite (**Fig. 4c-V**), and rare

401   very fine-grained pyrrhotite that is identified by the Fe-S ratio in EDX analyses (**Fig. 4c-IV and Fig. S8**).

402   Furthermore, Mn- and Fe-rich carbonate minerals are also observed in several areas (**Fig 4c-IV to VI, Fig

403   S7 and S8**). Pyrite is not observed.

404   Associated with the fracture surface, there is a ~1-cm thick weathering profile that is detectable by the

405   absence of sulfide minerals, carbonate minerals, and chlorite, and the presence of different accessory

406   minerals. In unweathered rock, Mn is predominantly hosted in carbonate minerals with additional

407   incorporation in chlorite, whereas in weathered areas Mn is absented and Fe oxides, Fe-oxyhydroxides

408   and/or Fe-(oxyhydr)oxide-sulfates (from now Fe-oxide) are pervasive and forms pseudomorphs of the

409   replaced minerals (i.e., sulfide minerals, **Figs. 4c-II and S7**).

410   In addition, a layer of Fe-oxides approximately 30 µm thick covers the fracture surface (**Figs. 4b and

411   S7**). This coating is virtually pure Fe-oxide, with a final Mn oxides coat formed over the Fe precipitates,

412   but lacking quartz or clay minerals. The expected Fe- and Mn-mineral phases are goethite and pyrolusite,

413   respectively, which would be in equilibrium at the groundwater conditions (Bladh, 1982; Post, 1999;

414   Manning et al., 2020). The coating exhibits interior banding in the BSE image concomitant with

415   variations in O intensity, but not in the Fe or Mn elemental maps (**Fig. 4b and S7**).

416   *3.2.2. µXRF and µXANES Analysis*

417   Elemental distribution maps, integrated profiles of major and trace elements (**Fig. 5**), and trends in the

418   oxidation states of iron (**Fig. 6a**) reveal a weathering profile with two distinct weathering fronts (located

419   at ~3 and ~7 mm from the fracture surface) that divide the profile into three zones (A, B and C)

420   characterized by different compositions. Zone C is the deepest and the least weathered area of the profile

421   where sphalerite is confirmed by S K-edge μXANES and EDX (**Fig. S8 and S9**); the sphalerite also

422   contains Se and Fe (**Fig. 5**). Iron K-edge μXANES from two locations in Zone C (spot 10 and 11, both

423   ~8.5 mm from the fracture surface, **Fig. 6 and S9**) do not match any single reference, however LCF point

424   to the presence of Fe(II)-chlorite and siderite **(Fig. 6 and S9)**, in agreement with XRD and EDX

425   observations**.** The weathering front, at a distance of ~7 mm from the surface and highlighted by a green

426   triangle in **Fig. 5a,** demarcates the unweathered region that contains discrete particles of sphalerite and

427   the weathered area where sphalerite is absent. This weathering profile thus represents the front in the

428   oxidative weathering of sulfide minerals and marks the division between weathered (Zones A and B) and

429   unweathered rock (Zone C).

430   Zone B is a partially weathered area that lacks sphalerite, shows a gradient in Mn, and contains Ca-

431   rich minerals that SEM-EDX data indicate are likely calcite. Zone A is the closest to the fracture, and

432   most affected by weathering reactions that result in a loss of chlorite and sulfide minerals. The transition

433   between Zones A and B occurs approximately 3 mm from the fracture surface and is shown by a blue

434   triangle in **Fig. 5a**. It is defined by the calcite dissolution front inferred from the Ca distribution in μXRF

435   mapping and SEM-EDX observations. Beneath this position, the Ca K-edge map (**Fig. 5a**) shown that Ca

436   is concentrated in discrete areas (i.e., calcite grains). Above this position, calcite grains are absent, and Ca

437   is distributed in a homogeneous background. Zone B shows a gradual loss of Mn towards the fracture

438   surface (**Fig. 5a**) that is mirrored by a transition in Fe oxidation state from Fe(II) to Fe(III) (**Fig. 6a**). LCF

439   of Fe K-edge μXANESs from two locations (~4 and ~4.5 mm from the fracture surface) indicate the

440   presence of chlorite (Muñoz et al., 2006) **(Fig. 6 and S9)**, suggesting that this mineral is not affected by

441   weathering in Zone B. Iron K-edge μXANES from different locations in the weathered region (Zones A

442   and B) are consistent with goethite **(Fig. 6, and S9)**. In addition, S K-edge XANES spectra and Fe

443   suggest the presence of hydrous Fe-sulfate minerals such as jarosite in Zone A and B **(Fig. 7, S9)**

444   (Bigham and Nordstrom, 2000).

445   *3.2.3. Rock Magnetic Analyses*

446   Low-temperature rock magnetic experiments on samples from the four slices cut parallel to weathered

447   fracture surface at 3.3 m bgs (**Fig. 3**) reveal a large difference in the ferromagnetic mineral composition in

448   the unweathered rock relative to the weathered rock close to the fracture (**Fig. 8a**). The slice that is

449   furthest from the fracture surface (> 10 mm) contains magnetite, pyrrhotite, and siderite. In contrast, the

450   dark ochreous slice at the fracture is dominated by goethite, identified by a large progressive decrease in

451 remanent magnetism during LTSIRM warming curves with higher remanence seen in FC LTSIRM

452 experiments than ZFC LTSIRM experiments (Guyodo et al., 2003; Liu et al., 2006). The rate of decrease

453 upon warming can change based on elemental impurities and grain size, with smaller grain sizes having a

454 larger decrease (Dekker, 1989; Maher et al., 2004). The difference-spread between the FC and ZFC

455 LTSRIM will also increase with decreasing grain size until grains become superparamagnetic in size

456 (Guyodo et al., 2003, 2006; Lagroix and Guyodo, 2017). Based on these trends, we interpreted that at

457 least some of the measured goethite at the fracture is sub-micron (nanophase) in size.

458   Rock slices contain an increasing amount of goethite as they get closer to the fracture surface,

459 whereas pyrrhotite and magnetite decrease in abundance. Although pyrrhotite is not detectable in the

460 RTSIRM and LTSIRM data from the fracture surface sample, as goethite dominate the low-temperature

461 behavior and the Besnus transition is not visible (e.g., Swanson-Hysell et al., 2012), RRM measurements

462 suggest pyrrhotite could be still present with $B_{eff} > \pm 20$ µT at 5 rps (Potter and Stephenson, 1986; Suzuki

463 et al., 2006) (**Fig. S10**). Siderite is not found in all samples containing goethite.

464   Room temperature coercivity experiments on the same slices from the fracture surface at 3.3 m bgs

465 also show trends with distance from the fracture and associated weathering intensity (**Fig. 8b**). The loss of

466 the high-moderate coercivity contribution (attributed to pyrrhotite) is consistent with the profile in the

467 oxidative weathering of sulfide minerals using SEM, µXRF and low-temperature magnetic methods. The

468 presence of goethite associated with the loss of pyrrhotite cannot be easily probed with room temperature

469 rock magnetic data because the coercivity range for goethite is above the range probed using IRM

470 demagnetization data. However, the sample closest to the fracture (STOP) shows a very high-coercivity

471 component using the noisier DC demagnetization curves corroborating insights from low-temperature

472 analyses **(Fig. S11)** (Peter and Dekkers, 2003).

4. DISCUSSION

474   The whole rock mineralogical and geochemical profiles in the 36-m Redwell Basin core display sharp

475 variations that indicate a complex geological history where hydrothermal activity increased the

476 heterogeneity of the original sedimentary rock. On the contrary, weathering-related mineralogical and

477 geochemical transformation homogenized the affected rocks. Weathering occurs dominantly at fracture

478 surfaces, indicating that groundwater flow through the relatively impermeable host rocks was fractured

479 controlled. The integration of bulk rock analysis, X-ray, electron, and optical microscopy with magnetic

480 measurements provided complementary support for key mineral reactions and products We discuss the

481 results from our study to propose a geochemical model for fracture-controlled and whole rock weathering,

482 that we present below. In addition, although only present as trace mineral phases, the widespread

483   distribution of pyrrhotite and siderite suggests a role for these reactive phases as indicators of the extent

484   of rock weathering.

485   **4.1. Bulk Hydrothermal Alteration and Weathering of Host Rock**

486   The XRD and chemical analyses indicate that the most abundant minerals in the Mesaverde

487   Formation are quartz, feldspar (albite and orthoclase) and chlorite, in agreement with previous

488   descriptions (Gaskill et al., 1967) **(Fig. 2)**. However, clay minerals are abundant, particularly illite and

489   muscovite, whereas the feldspar concentration is lower in all samples with respect to standards value for

490   Mesaverde Formation. These clay minerals commonly occurred in marine sedimentary formations such as

491   the underlying Mancos Shale and in hydrothermal alteration assemblages associated with porphyry

492   deposits (Seedorff et al., 2005; Taylor and Macquaker, 2014). At Redwell Basin, magmatic hydrothermal

493   processes altered sedimentary and diagenetic minerals, such as feldspar, into clay minerals as part of

494   widespread propylitic and sericitic hydrothermal alteration related to porphyry Mo mineralization

495   (Thomas and Galey, 1982). Pyrite also formed during hydrothermal activity, filling veins and forming

496   common and widespread dissemination in the host rocks **(Fig. S3)**.

497   Among the bulk samples of the MW1 drill core analyzed by all techniques, the samples at 2 and

498   27.3 m bgs exhibit the simplest bulk mineralogy and contain the lowest concentration of Zn, Cu and other

499   metals (**Fig. 2 and 3**). In the case of sample at 27.3 m bgs, the observed chemical and mineralogical

500   association suggest that it was the least hydrothermally altered and thus closest to parent rock. Although

501   feldspar minerals are not detected by XRD, probably as a consequence of particular sedimentary

502   conditions due to the low level of hydrothermal alteration at this depth. This sample also has the lowest

503   overall remanent magnetism and contains magnetite and hematite. Magnetite is a common detrital mineral

504   in sedimentary rocks (Maher, 2011) and can also form authigenically through clay mineral diagenesis

505   (Lovley et al., 1987; Maher and Taylor, 1988; Kopp and Kirschvink, 2008; Kars et al., 2015). Due to its

506   prevalence throughout the MW1 drill core, we posit that much of magnetite within this system was

507   detrital or possibly early diagenetic and was preserved in low abundances (order of 0.001% wt). The

508   exception is sample at 18.3 m bgs, where the strong magnetization suggests an increase in abundance of

509   ferromagnetic phases, likely an increase in magnetite due to its strong saturation magnetization (Peter and

510   Dekkers, 2003); we interpret that in this case the low-coercivity component is hydrothermal magnetite

511   which formed in place of pyrrhotite during hydrothermal alteration (with the less likely possibility being a

512   unique detrital composition during deposition).

513   The bulk rock data for the sample at 2 m bgs displays the effects of weathering. This sample is

514   composed of unconsolidated, ochre-colored fragments, with the enrichment of goethite, the greatest

515   concentration of clay minerals, and the depletion of sulfide minerals and feldspar. Hence, sulfide mineral

516   weathering generated goethite, and silicate mineral weathering formed kaolinite, vermiculite and illite

517　(**Fig. 2a, 4b and S4**). Ochre-colored fracture surfaces at other locations in the drill core reflect weathering

518　at greater depth (*e.g.*, at 7 and 10 m bgs). Due to the small rock volume affected, however, the

519　consequences of weathering are not detectable by bulk elemental or mineralogical analyses, requiring the

520　implementation of higher-spatial-resolution methods to determine weathering reaction pathways.

521　　　　　Magnetic measurements show that Fe(II) phases siderite or pyrrhotite are common in

522　unweathered rock, although present at low concentration, but their absence from the sample at 27.3 m bgs

523　suggests that these phases are not present in the sedimentary rock and are restricted to zones of

524　hydrothermal alteration. Although modern examples of detrital pyrrhotite and early diagenetic pyrrhotite

525　have been found in unique environments (Horng and Roberts, 2006; Larrasoana et al., 2007), most

526　pyrrhotite forms directly in hydrothermal deposits, or as a result of low-temperature prograde

527　metamorphism, where the loss of sulfur from pyrite formed pyrrhotite (Kissin and Scott, 1982; Hall,

528　1986; Craig and Vokes, 1993; Elmore et al., 2012). Siderite is absent in the deepest sample (**Fig. 3a**), but

529　a magnetic signature interpreted to be rhodochrosite (Mn carbonate) is instead present (Frederich et al.,

530　2003) as supported by SEM data. As discussed below, although only present as trace mineral phases, the

531　widespread distribution of pyrrhotite and siderite suggests a role for these reactive phases as indicators of

532　the extent of rock weathering.

4.2. Fracture-Scale Observations of Weathering

534　　　Microscale analysis of the fracture weathering profile at 3.3 m bgs by SEM, µXRF and µXANES

535　(**Figs. 4 to 7**) provides information on mineral transformations and the redistribution and net loss or net

536　gain of elements within the weathering profile. In **Figure 5**, the average fluorescence emission counts

537　(i.e., Fe, Mn, Ca, Si, Al and K) or median counts (i.e., S, Se and Zn) above and below the 7-mm

538　(transition between Zone B and C) are plotted on top of the elemental profiles to assess whether mass

539　balance is maintained during weathering. Iron and Ca show a similar average value above and below the

540　second weathering front, even considering the high Fe accumulation at the fracture surface. Hence, Fe

541　released during chlorite and Fe-bearing sphalerite dissolution, was transported towards the fracture

542　surface but reprecipitated without loss to groundwater. The conclusion that the Fe surface coating was

543　generated from the rock and not deposited from groundwater is consistent with the groundwater pH (~7.5)

544　because Fe-oxide phases are highly insoluble at pH 5. The banding of the coating could suggest that trace

545　element chemistry controls the compositional banding. The low concentration of these elements prevents

546　their detection by EDX. However, the weight and valence differences between trace elements with Fe and

547　Mn would change the ratio metal-oxygen, explaining the bands observed in O map (**Fig. 4b-I**). The Fe-

548　enriched layer at 3 to 3.5 mm, highlighted by square bracket symbol in **Fig. 5b**, is interpreted as a

549　microfracture that served as a conduit for groundwater and additional localized weathering.

550   Two elements, Mn and Si display clear evidence of net loss to groundwater. Manganese is depleted

551   from the fully weathered Zone A, although partially redeposited in the Fe-rich coating. According to

552   SEM-EDX, Mn is mainly found as Mn-rich calcite; therefore, it makes sense that both Ca and Mn are

553   found at the same depth, although Mn is more mobile than Ca. This front indicate the position in which

554   carbonate minerals were totally dissolved, neutralizing the acidity generated by sulfide mineral

555   dissolution, Fe(II) oxidation to Fe(III), and Fe-oxide precipitation. Silicon is depleted within ~300 µm at

556   the fracture surface. Several elements, Zn, S, Se (**Fig. 5**) are enriched at the fracture surface. Zinc occurs

557   at a greater concentration than in unweathered rock, indicating deposition from groundwater, likely

558   through sorption to, or coprecipitation in, Fe(III) precipitates. The co-location of Se with Zn and S (**Fig.**

559   **5**) suggest that, in this sample, Se is dominantly hosted by sphalerite in the unweathered rock. but the

560   mass balance for S, Zn and Se is difficult to assess due to the small numbers of particulate source

561   minerals in the unweathered Zone C.

562   The weathering zone is enriched in Al and K, whose concentrations increase toward the fracture

563   surface, suggesting that fine-grained mica is formed as product of feldspar weathering, which is also

564   consistent with Si depletion, following the equation:

565      $3\ NaAlSi_3O_8 + K^+ + 2\ H^+ + 2H_2O => KAl_3Si_3O_{10}(OH)_2 + 3\ Na^+ + 6\ H_4SiO_4$ (2)
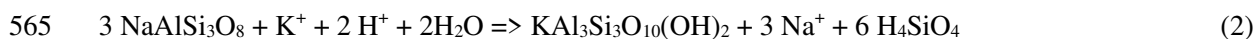
566   The consumption of protons in equation 2 indicates that silicate dissolution consumes acidity

567   generated by sulfide minerals oxidation in a neutralization reaction. The presence of dissolution textures

568   throughout the profile indicate that weathering reactions were superimposed over a complex hydrothermal

569   alteration mineral assemblage. The observation of Fe-oxide mineral precipitates around feldspar grains

570   with dissolution pits, found uniquely in Zones A and B (**Fig. 4c-III**), strongly indicates that feldspar

571   dissolution neutralized acidity generated by Fe(II) oxidation to Fe(III) and Fe-oxide precipitation. Silicate

572   dissolution is slower than carbonate mineral dissolution but likely contributes to acidity neutralization

573   long after carbonate minerals are fully consumed.

574   Surprisingly, pyrite is not observed in optical, electron or X-ray analyses of any of our samples even

575   though hand sample observations showed it to be the most abundant sulfide mineral in the MW1 core,

576   and it is detected by XRD in many samples (**Fig. 2a**). Either pyrite was not formed in the rock at the

577   analyzed locations, or it was preferentially oxidized in the weathering profile before other sulfide

578   minerals such as sphalerite. In either case, pyrite oxidation is a potential source of remobilized Fe. Taken

579   together, all analytical data suggest that the weathering reactions in Zones A and B involved the total or

580   partial dissolution of sulfide minerals (i.e., pyrite, sphalerite and pyrrhotite), carbonate minerals (i.e.,

581   calcite, Mn-bearing calcite and siderite), as well as the acid-promoted total or partial dissolution of

582   silicate minerals (i.e., chlorite and feldspar).

583   SEM imaging show that weathering reactions caused a net increase in rock pore volume with clear

584   differences between locations close to the fracture surface (**Fig. 4b-I** to **Fig. 4c-III**) and those in the

585   unweathered rock (**Fig. 4c-IV** to **Fig. 4c-VII**). Specially, the presence of void space between unweathered

586   minerals at the fracture surface is clear, whereas the unweathered rock lacks these holes and spaces. This

587   increasing porosity could be the consequence of (1) dissolution of reactive minerals such as carbonate

588   minerals, or (2) volume change during mineral replacement reactions. Therefore, weathering increased

589   the porosity in areas closer to the fracture, thereby enhancing the diffusion of reactive species in pore

590   water toward the unweathered rock.

591   **4.3. Cross-Scale Mineral Signatures of Weathering Extent**

592   The weathering reactions described in detail at the weathering profile at 3.3 m bgs may be

593   extrapolated to explain the observed mineral assemblage resulting from weathering at the drill core scale.

594   Magnetic analysis of rock slices at fracture scale revealed transitions in Fe mineralogy attributable to

595   weathering (**Fig. 8**). The low-temperature data indicate that weathering caused a loss of magnetite,

596   pyrrhotite, and siderite. The room-temperature coercivity measurements at this depth are consistent with

597   the loss of magnetite and pyrrhotite. A shift in the moderate coercivity peak is noted from the

598   unweathered to the weathered sandstone samples suggesting a preferential weathering of minerals with

599   lower coercivity, potentially very large or very small magnetite grains (Dunlop, 1986; Egli, 2004) **(Fig.**

600   **S11)**. In addition, weathering was associated with the formation of goethite, at least some of which is

601   nanometric, as evidenced in the low-temperature magnetic and Fe K-edge μXANES data (**Fig. 6b**).

602   Siderite also weathered rapidly with a sharp transition noted between the unweathered and weathered rock

603   (~ 10mm from the fracture surface) above which siderite is not detected and goethite appears. These

604   observations agree with the SEM-EDX results, displaying both pyrrhotite and siderite mineral in the least

605   weathered area only (**Fig. 4c-IV to 4c-VII**). These trends are partially repeated in the weathering profile

606   at 10 m bgs, where a small decrease in moderate coercivity component (magnetite) accompanies the

607   complete loss of a high-moderate coercivity component (pyrrhotite). No pyrrhotite and weatherable

608   magnetite are detected in the fracture at 7 m bgs, suggesting that this sample was more fully weathered

609   than anticipated by visual inspection (**Fig. 8 and S12**). Therefore, magnetite, siderite and pyrrhotite can

610   be included in the list of minerals affected by weathering, contributing to the total Fe that is initially

611   remobilized by oxidation and subsequently retained by goethite precipitation.

612   Magnetic measurements at the meter-scale are consistent with fracture-scale results. Bulk samples

613   below 2.6 m bgs display pyrrhotite and/or siderite except in those less affected by hydrothermal activity

614   (i.e., 27.3 m bgs, **Fig 3**), whereas the shallowest and the most weathered samples contain only

615   goethite/hematite and the moderate-coercivity component. Therefore, the anticorrelation between

616   ferromagnetic minerals, especially pyrrhotite, and goethite abundance could be used as a proxy to indicate

617 weathering intensity in mineralized rocks at any scale. These observations also indicate that the
618 mineralogical and chemical heterogeneity imposed by hydrothermal alteration were at least partially
619 homogenized by weathering reactions as, for example, pyrite, pyrrhotite, siderite, and Fe(II)-chlorite
620 weathering all led to the precipitation of Fe-oxide (mostly goethite).

621   Silicate minerals also showed analogous trends in fracture- and core-scale data. The depletion of
622 feldspar and chlorite, and the increase in illite and muscovite observed in shallower samples at drill core
623 MW1 (**Fig. 2**) reflects the replacement of feldspar with sericite observed in the fracture weathering
624 profiles at 3.3 m bgs (**Fig 4c-III**) as described by reaction (2). The high clay mineral and low feldspar
625 concentrations throughout the drill core could be interpreted as the effect of hydrothermal alteration (**Fig.
626 2**). Both hydrothermal and acidic conditions could cause the dissolution textures observed in feldspar at
627 the microscale (**Fig. 4c-III**). However, the increasing clay mineral content toward the surface (both the
628 fracture surface and the top of the drill core) shows the contribution of weathering to reaction (2).

629   The S content and carbonate mineral estimation indicate that only bulk core samples above 2.6 m bgs
630 lack sulfides and carbonates (**Fig. 2 and Table S1**). Similar trends are observed by SEM-EDX and μXRF
631 mapping, where the less weathered regions at fracture scale (Zone C) display both carbonate and sulfide
632 minerals, which gradually disappear toward Zone A (**Fig. 4 to 7**). The fracture-scale data additionally
633 show that pyrite oxidation precedes carbonate dissolution and hence indicate that carbonate dissolution
634 neutralizes acidity generated by sulfide oxidation.

635   The behavior of trace elements such as Se is more difficult to compare between scales. Selenium was
636 released from sulfide minerals and, at the fracture scale, it was redistributed but overall retained within
637 the weathered region, likely through sorption or co-precipitation (Peak and Sparks, 2002; Sherman and
638 Randall, 2003). The ability of Fe-oxides to retain trace elements at sites impacted by sulfidic rock
639 weathering is well-documented (e.g., Gunsinger et al., 2006; Holmstrom and Ohlander, 2001) (**Fig 5b**).
640 However, the Fe accumulation above 2.6 m bgs at drill core MW1 is not correlated with elevated Se
641 concentration, which is in contrast totally depleted. Similar differences are observed for Zn, which may
642 indicate that some differences in weathering reaction happened between scales, for example, the influence
643 of organic reaction near ground surface (Hasenmueller et al., 2017; Hubbard et al., 2018).

644   In summary, most of the mineral reactions and element trends associated with weathering can be
645 identified at both the core and fracture scales. Samples nearest the top of MW1 drill core (i.e., 2 and 2.6 m
646 bgs) are highly weathered with similar mineral composition as Zone A at fracture scale. Similarly, the
647 drill core section partially weathered displays weathering profiles around fractures (i.e., from 2.6 to 10 m
648 bgs, **Fig. 8**) and could be correlated to Zone B at the fracture scale. Finally, the core section below 10 m
649 bgs is least weathered and can be correlated with Zone C at the fracture scale. The development of a

650 plausible geochemical model for weathering, however, is most accurately obtained through the analysis of

651 fracture-scale data.

4.4. Conceptual Model

653   The results obtained in this research allow a geochemical model to be developed describing the

654 principal mineral and elemental transformations and element mobility (**Fig. 9**). This model displays the

655 general weathering reactions identified at both scales, and could be adapted to local variation in

656 parameters as mineralogical variation (e.g., absence of pyrite) and changes in the rock structure (e.g.,

657 fracture density). Iron was mostly released at MW1 by oxidation of pyrite, but also by the weathering of

658 chlorite, Fe-rich sphalerite, siderite, pyrrhotite and magnetite (**Fig 2 to 8**). Iron transport was accompanied

659 by precipitation of jarosite (an Fe-oxyhydroxide sulfate, **Fig. 2 and 7**), and goethite (**Fig. 3, 6 and 8**). At

660 the fracture scale, the presence of the stable mineral phase jarosite, which preferentially forms at pH

661 values below 2.5 in the presence of Fe(III) and sulfate (Bigham et al., 1996), suggesting acid pore water.

662 At higher pH in pore water, the metastable phase schwertmannite forms more readily than jarosite, but

663 recrystallizes over months to form goethite whereas liberating sulfate (Bigham et al., 1996; Acero et al.,

664 2006). In such acidic pore water, both Fe^{+2} and Fe^{+3} species are mobile (Bigham and Nordstrom, 2000)

665 and the detection of some Fe(II) in the surface coating is consistent with at least part of the Fe diffusing as

666 Fe^{+2} to the fracture (**Fig. 6**). The sorption of soluble Fe(II) to goethite and solid-state electron transfer

667 could provide a mechanism for long-term stabilization of Fe(II) (Williams and Scherer, 2004; Handler et

668 al., 2009). The increasing Fe content towards the fracture and the coating of goethite along the fracture

669 are consistent with the neutralization of acidic pore water as it mixes with the circumneutral groundwater

670 at MW1 (Manning et al., 2020). Although a goethite coating could form by precipitation of Fe from over-

671 saturated groundwater (Parviainen et al., 2015), the overall mass conservation of Fe strongly indicates

672 that all the coating originated from local weathering reactions inside the rock (**Fig. 5**). These reactions

673 may be extrapolated to the meter-scale, where the ochreous precipitates coating the host rock, the jarosite

674 and goethite detection by XRD and magnetism, respectively, and the high Fe accumulation with respect

675 to the parent rock at the top of the drill core indicate that Fe was retained after weathering of the host rock

676 in MW1 (**Figs. 2, 3 and S2**).

677   The oxidation of pyrite and Fe-rich sphalerite were the two reactions that generated acidity (Moncur

678 et al., 2009; Çelebi and Öncel, 2016), which was partially neutralized by the complete dissolution of

679 carbonate minerals (calcite, Mn-bearing calcite and siderite) and the partial dissolution of reactive silicate

680 minerals (feldspar and chlorite) remaining from prior hydrothermal alteration. The elevated relative

681 abundances of K and Al near the fracture and the anticorrelation between feldspar and clay minerals

682 content at the drill core are consistent with clay mineral formation resulting from acid-promoted feldspar

683 and chlorite dissolution and subsequent clay mineral precipitation (kaolinite, illite, muscovite and

684   vermiculite, **Fig 2, 5, 6 and 7**). Sphalerite oxidation was also the source of Zn that, in contrast to Fe, was

685   mostly lost from the weathered rock (**Fig. 2b and 5**). Secondary Zn phases could not be identified and

686   only a diffuse distribution associated with Fe suggests that Zn was partially co-precipitated with, or

687   adsorbed onto Fe(III)-phase products (Waychunas et al., 2005). Manganese was also mainly lost from the

688   weathering rock and partially accumulated on top or within Fe coatings (**Fig 2b and 5**). The sharp

689   weathering profile observed at fracture scale is consistent with diffusion-limited dissolution of carbonate

690   minerals, neutralizing pH in pore water (**Fig 5**). The retention of some Mn-oxide as pyrolusite on the

691   goethite fracture coating, which requires slightly acid to neutral pH (Post, 1999), supports the conclusion

692   of a strong pH gradient between the pore water in the rock and the groundwater in the fracture. Because

693   these pyrolusite precipitates are sparse, Mn mobility may be controlled by seasonal variations in pH and

694   dissolved inorganic carbon (Sullivan et al., 2016; Hubbard et al., 2018). Seasonal variation might explain

695   the layered texture of the surface coating evident at the SEM if the Fe-phases were weathered following

696   precipitation by changes in groundwater chemistry (Cruz-Hernández et al., 2019) (**Fig. 4b**). However, X-

697   ray microprobe and magnetic measurements are dominated by goethite, so the banding could be also

698   attributed to variation in density due to the content of trace elements (**Fig. 7 and 8**). Although pyrolusite

699   is not detected in the shallowest samples in MW1, Mn accumulation with respect to parent rock and

700   circumneutral groundwater pH are also consistent with pyrolusite precipitation and/or sorption into Fe-

701   oxides minerals.

702   **5. CONCLUSIONS**

703   The coupled geochemical, X-ray spectromicroscopy and rock magnetic data in this study support a

704   conceptual model for the weathering of sulfidic sedimentary rocks that follows a common geochemical

705   pattern. Specifically, the abundance of sulfide mineral controls the generation of acidity and dissolved

706   elements, the abundance of neutralizing minerals determines the pore-fluid pH, and pH-dependent

707   mobility of dissolved elements controls their transport to the groundwater. This model likely holds

708   regardless of the source of the disseminated sulfide minerals (e.g., hydrothermal alteration or diagenesis)

709   and the nature of the neutralizing mineral phases (i.e., carbonate minerals, chlorite, and feldspar).

710   This study concludes that weathering at the studied location and depth made little contribution to the

711   export of acidity and metals, which is consistent with prior field and simulation studies in many regions

712   of the Redwell Basin (Kimball et al., 2010). Therefore, the acid drainage that occurs in the Redwell Basin

713   was not a consequence of weathering throughout the basin itself. It was likely the result of the weathering

714   in highly mineralized areas, where the acidity generated by pyrite and Fe oxidation cannot be totally

715   neutralized by carbonate and silicate minerals dissolution, as well as acid pore water dilution by mixing

716   with circumneutral groundwater. The data presented here from the Redwell Basin should be compared

717 with those from other areas where rocks with high pyrite concentration are affected by weathering, to
718 refine this conceptual model and application to other systems with different sulfide mineral content.

719   The conceptual model of **Figure 9** could also provide a basis for understanding past and future
720 weathering processes throughout the sandstone sequences of the MW1 drill core, provided that variations
721 in abundance of mineral phases abundance are considered. Predicting the potential metal exports from the
722 rock as the active weathering front descends is challenging, because phases as such as sphalerite,
723 observed by synchrotron microfocused X-ray spectromicroscopy, were never detected using bulk XRD.
724 However, magnetic data track the loss of the sulfide pyrrhotite and the formation of goethite in the well-
725 studied fracture surface at 3.3 m bgs and at core scale. These paired magnetic measurements thus could
726 offer a proxy for weathering extent in hydrothermally altered sulfidic rock.

747

748 **Appendix A: Supporting material:** (1) Geographic map of the Colorado River Basin, (2) Photographs
749 of MW1 core boxes with indication of sample location, (3) The geological description of the core MW1,

750 (4) XRD of clay mineral fractions, (5) Coercivity spectra from all unweathered samples from core MW1,

751 (6) Details of the weathering profile location at 3.3 m depth in core MW1. (7) Elemental maps obtained

752 with EDX at 3.3 m MW1 weathering profile, (8) Elemental composition of selected spots by EDX, (9)

753 All Fe K-edge and S K-edge XANES spectra collected at 3.3 m bgs MW1 weathering profile, including

754 corresponding best LCF of Fe K-edge fits, (10) Rotational remanent magnetization data, (11-12)

755 Coercivity spectra of rock slices at weathering fracture surfaces from other depths in the MW1 core and

756 (Table S1 and S2) Major and trace elemental composition in core MW1.

757

REFERENCES

Acero P., Ayora C., Torrentó C. and Nieto J. M. (2006) The behavior of trace elements during schwertmannite precipitation and subsequent transformation into goethite and jarosite. *Geochim. Cosmochim. Acta* **70**, 4130–4139.

Alford L., Gysi A. P., Hurtig N. C., Monecke T. and Pfaff K. (2020) Porphyry-related polymetallic Au-Ag vein deposit in the Central City district, Colorado: Mineral paragenesis and pyrite trace element chemistry. *Ore Geol. Rev.* **119**, 103295.

Anderson S. P., Dietrich W. E. and Brimhall G. H. (2002) Weathering profiles, mass-balance analysis, and rates of solute loss: Linkages between weathering and erosion in a small, steep catchment. *Bull. Geol. Soc. Am.* **114**, 1143–1158.

Bao Z., Al T., Bain J., Shrimpton H. K., Finfrock Y. Z., Ptacek C. J. and Blowes D. W. (2022) Sphalerite weathering and controls on Zn and Cd migration in mine waste rock: An integrated study from the molecular scale to the field scale. *Geochim. Cosmochim. Acta* **318**, 1–18.

Berquo T. S., Banerjee S. K., Ford R. G., Penn R. L. and Pichler T. (2007) High crystallinity Si-ferrihydrite: An insight into its Néel temperature and size dependence of magnetic properties. *J. Geophys. Res.* **112**, 1–12.

Besnus M. and Meyer A. (1964) Nouvelles données expérimentales sur le magnétisme de la pyrrhotine naturelle. In *Conference of Magnetism, Nottingham*

Bigham J. M. and Nordstrom D. K. (2000) Iron and aluminum hydroxysulfates from acid sulfate waters. *Rev. Mineral. Geochemistry* **40**, 351–403.

Bigham J. M., Schwertmann U., Traina S. J., Winland R. L. and Wolf M. (1996) Schwertmannite and the chemical modeling of iron in acid sulfate waters. *Geochim. Cosmochim. Acta* **60**, 2111–2121.

Bladh K. W. (1982) The formation of goethite, jarosite, and alunite during the weathering of sulfide-bearing felsic rocks. *Econ. Geol.* **77**, 176–184.

Blodau C. (2006) A review of acidity generation and consumption in acidic coal mine lakes and their watersheds. *Sci. Total Environ.* **369**, 307–332.

Bondu R., Cloutier V., Rosa E. and Benzaazoua M. (2016) A review and evaluation of the impacts of climate change on geogenic arsenic in groundwater from fractured bedrock aquifers. *Water. Air. Soil Pollut.* **227**, 296.

786   Brantley S. L. and Lebedeva M. (2011) Learning to read the chemistry of regolith to understand the critical zone.

787   *Annu. Rev. Earth Planet. Sci.* **39**, 387–416.

788   Brimhall G. H. and Dietrich W. E. (1987) Constitutive mass balance relations between chemical composition,

789   volume, density, porosity, and strain in metasomatic hydrochemical systems: Results on weathering and

790   pedogenesis. *Geochim. Cosmochim. Acta* **51**, 567–587.

791   Buss H. L., Sak P. B., Webb S. M. and Brantley S. L. (2008) Weathering of the Rio Blanco quartz diorite, Luquillo

792   Mountains, Puerto Rico: Coupling oxidation, dissolution, and fracturing. *Geochim. Cosmochim. Acta* **72**,

793   4488–4507.

794   Çelebi E. E. and Öncel M. S. (2016) Determination of acid forming potential of massive sulfide minerals and the

795   tailings situated in lead/zinc mining district of Balya (NW Turkey). *J. African Earth Sci.* **124**, 487–496.

796   Chapin C. E. (2012) Origin of the Colorado Mineral Belt. *Geosphere* **8**, 28–43.

797   Chevrier V., Mathé P., Rochette P. and Gunnlaugsson H. P. (2006) Magnetic study of an Antarctic weathering

798   profile on basalt : Implications for recent weathering on Mars. *Earth Planet. Sci. Lett.* **244**, 501–514.

799   Chung F. H. (1974) Quantitative interpretation of X-ray diffraction patterns of mixtures. I. Matrix-flushing method

800   for quantitative multicomponent analysis. *J. Appl. Crystallogr.* **7**, 519–525.

801   Craig J. R. and Vokes F. M. (1993) The metamorphism of pyrite and pyritic ores: an overview. *Mineral. Mag.* **57**,

802   3–18.

803   Cruz-Hernández P., Carrero S., Pérez-López R., Fernandez-Martinez A., Lindsay M. B. J., Dejoie C. and Nieto J. M.

804   (2019) Influence of As(V) on precipitation and transformation of schwertmannite in acid mine drainage-

805   impacted waters. *Eur. J. Mineral.* **31**, 237–245.

806   Dekker M. (1989) Magnetic properties of natural goethite—II. TRM behaviour during thermal and alternating field

807   demagnetization and low-temperature treatment. *Geophys. J. Int.* **97**, 341–355.

808   Dessert C., Dupré B., Gaillardet J., François L. M. and Allègre C. J. (2003) Basalt weathering laws and the impact

809   of basalt weathering on the global carbon cycle. *Chem. Geol.* **202**, 257–273.

810   Dunlop D. J. (1986) Hysteresis properties of magnetite and their dependence on particle size: A test of pseudo-

811   single-domain remanence models. *J. Geophys. Res.* **91**, 9569–9584.

812   Egli R. (2004) Characterization of individual rock magnetic components by analysis of remanence curves, 1.

813   Unmixing natural sediments. *StGG* **48**, 391–446.

814   Elmore R. D., Muxworthy A. R. and Aldana M. (2012) Remagnetization and chemical alteration of sedimentary

815   rocks. *Geolofical Soc. London, Spec. Publ.* **371**, 1–21.

816   Essalhi M., Sizaret S., Barbanson L., Chen Y., Lagroix F., Demory F., Nieto J. M., Sáez R. and Capitán M. Á.

817   (2011) A case study of the internal structures of gossans and weathering processes in the Iberian Pyrite Belt

818   using magnetic fabrics and paleomagnetic dating. *Miner. Depos.* **46**, 981–999.

819   Frederich T., Von Dobeneck T., Bleil U. and Dekkers M. (2003) Towards the identification of siderite,

820   rhodochrosite, and vivianite in sediments by their low-temperature magnetic properties. *Phys. Chem. Earth,*

821   *Parts A/B/C* **28**, 669–679.

822   Gaillardet J., Dupré B., Louvat P. and Allègre C. J. (1999) Global silicate weathering and CO2 consumption rates

823   deduced from the chemistry of large rivers. *Chem. Geol.* **159**, 3–30.

824   Gaskill D. L., Godwin L. H. and Mutschler F. E. (1967) Geologic map of the Oh-be-Joyful quadrangle, Gunnison

825   county, Colorado. *U.S Geol. Surv.* **Map GQ-578**.

826   Gaste-Rector S. D. and Blanton T. N. (2019) The powder diffraction file: A quality materials characterization

827   database. *Powder Diffr.* **34**, 352–360.

828   Gray N. F. (1998) Acid mine drainage composition and the implications for its impact on lotic systems. *Water Res.*

829   **32**, 2122–2134.

830   Gu X., Heaney P. J., Reis F. D. A. A. and Brantley S. L. (2020) Deep abiotic weathering of pyrite. *Science (80-.).*

831   **370**.

832   Gunsinger M. R., Ptacek C. J., Blowes S. W., Jambor J. L. and Moncur M. C. (2006) Mechanisms controlling acid

833   neutralization and metal mobility within a Ni-rich tailings impoundment. *Appl. Geochemistry* **721**, 1301–1321.

834   Guyodo Y., Lapara T. M., Anschutz A. J., Penn R. L., Banerjee S. K., Geiss C. E. and Zanner W. (2006) Rock

835   magnetic, chemical and bacterial community analysis of a modern soil from Nebraska. *Earth Planet. Sci. Lett.*

836   **251**, 168–178.

837   Guyodo Y., Mostrom A., Lee Penn R. and Banerjee S. K. (2003) From nanodots to nanorods: Oriented aggregation

838   and magnetic evolution of nanocrystalline goethite. *Geophys. Res. Lett.* **30**, 1512.

839   Hall A. J. (1986) Pyrite-pyrrhotine redox reactions in nature. *Mineral. Mag.* **50**, 223–229.

840   Handler R. M., Beard B. L., Johnson C. M. and Scherer M. M. (2009) Atom exchange between aqueous Fe(II) and

841   goethite: An Fe isotope tracer study. *Environ. Sci. Technol.* **43**, 1102–1107.

842   Hasenmueller E. A., Gu X., Weitzman J. N., Adams T. S., Stinchcomb G. E., Eissenstat D. M., Drohan P. J.,

843   Brantley S. L. and Kaye J. P. (2017) Weathering of rock to regolith: The activity of deep roots in bedrock

844   fractures. *Geoderma* **300**, 11–31.

845   Heller M. I., Lam P. J., Moffett J. W., Till C. P., Lee J. M., Toner B. M. and Marcus M. A. (2017) Accumulation of

846   Fe oxyhydroxides in the Peruvian oxygen deficient zone implies non-oxygen dependent Fe oxidation.

847   *Geochim. Cosmochim. Acta* **211**, 174–193.

848   Herndon E. M., Martínez C. E. and Brantley S. L. (2014) Spectroscopic (XANES/XRF) characterization of

849   contaminant manganese cycling in a temperate watershed. *Biogeochemistry* **121**, 505–517.

850   Hilton R. G. and West A. J. (2020) Mountains, erosion and the carbon cycle. *Nat. Rev. Earth Environ.* **1**, 284–299.

851   Holmstrom H. and Ohlander B. (2001) Layers rich in Fe- and Mn-oxyhydroxides formed at the tailings-pond water

852   interface, a possible trap for trace metals in flooded mine tailings. *J. Geochemical Explor.* **74**, 189–203.

853   Horng C. S. and Roberts A. P. (2006) Authigenic or detrital origin of pyrrhotite in sediments?: Resolving a

854   paleomagnetic conundrum. *Earth Planet. Sci. Lett.* **241**, 750–762.

855   Hubbard S. S., Williams K. H., Agarwal D., Banfield J., Beller H., Bouskill N., Brodie E., Carroll R., Dafflon B.,

856   Dwivedi D., Falco N., Faybishenko B., Maxwell R., Nico P., Steefel C., Steltzer H., Tokunaga T., Tran P. A.,

857   Wainwright H. and Varadharajan C. (2018) The East River, Colorado, watershed: A mountainous community

858   testbed for improving predictive understanding of multiscale hydrological–biogeochemical dynamics. *Vadose*

859   *Zo. J.* **17**, 180061.

860   Jin L., Rother G., Cole D. R., Mildner D. F. R., Duffy C. J. and Brantley S. L. (2011) Characterization of deep

861   weathering and nanoporosity development in shale - A neutron study. *Am. Mineral.* **96**, 498–512.

862   Kars M., Aubourg C. and Suárez-Ruiz I. (2015) Neoformed magnetic minerals as an indicator of moderate burial:

863   The key example of middle Paleozoic sedimentary rocks, West Virginia. *Am. Assoc. Pet. Geol. Bull.* **99**, 389–

864   401.

865   Kim Y. K., Son H. Y., Choi Y. S., Moon K.-S. and Sunwoo K. H. (2000) Magnetically soft and electrically resistive

866   CoNiFeS alloy films prepared by electrodeposition. *J. Appl. Phys.* **87**, 5413.

867   Kimball B. A., Runkel R. L., Wanty R. B. and Verplanck P. L. (2010) Reactive solute-transport simulation of pre-

868   mining metal concentrations in mine-impacted catchments: Redwell Basin, Colorado, USA. *Chem. Geol.* **269**,

869   124–136.

870   Kirschvink J. L., Kopp R. E., Raub T. D., Baumgartner C. T. and Holt J. W. (2008) Rapid, precise, and high-

871   sensitivity acquisition of paleomagnetic and rock-magnetic data: Development of a low-noise automatic

872   sample changing system for superconducting rock magnetometers. *Geochemistry, Geophys. Geosystems* **9**,

873   Q05Y01.

874   Kissin S. and Scott S. (1982) Phase relations involving pyrrhotite below 350 degrees C. *Econ. Geol.* **77**, 1739–1754.

875   Kopp R. E. and Kirschvink J. L. (2008) The identification and biogeochemical interpretation of fossil magnetotactic

876   bacteria. *Earth-Science Rev.* **86**, 42–61.

877   Kraft S., Stümpel J., Becker P. and Kuetgens U. (1996) High resolution x-ray absorption spectroscopy with absolute

878   energy calibration for the determination of absorption edge energies. *Rev. Sci. Instrum.* **67**, 681–687.

879   Kump L. R., Brantley S. L. and Arthur M. A. (2000) Chemical weathering, atmospheric CO_2 and climate. *Annu.*

880   *Rev. Earth Planet. Sci.* **28**, 611–667.

881   Lagroix F. and Guyodo Y. (2017) A new tool for separating the magnetic mineralogy of complex mineral

882   assemblages from low temperature magnetic behavior. *Front. Earth Sci.* **5**, 61.

883   Larrasoana J. C., Roberts R. J., Musgrave R. J., Gracia E., Pinera E., Vega M. and Martinez-Ruiz F. (2007)

884   Diagenetic formation of greigite and pyrrhotite in gas hydrate marine sedimentary systems. *Earth Planet. Sci.*

885   *Lett.* **261**, 350–366.

886   Liu Q., Roberts A. P., Larrasoaña J. C., Banerjee S. K., Guyodo Y., Tauxe L. and Oldfield F. (2012) Environmental

887   magnetism; principles and applications. *Rev. Geophys.* **50**, RG4002.

888   Liu Q., Yu Y., Torrent J., Roberts A. P., Pan Y. and Zhu R. (2006) Characteristic low-temperature magnetic

889   properties of aluminous goethite [α-(Fe, Al) OOH] explained. *J. Geophys. Res. Earth Surf.* **111**, B12S34.

890   Lovley D. R., Stolz J. F., Nord G. L. and Phillips E. J. (1987) Anaerobic production of magnetite by a dissimilatory

891   iron-reducing microorganism. *Nature* **330**, 252.

892   Maher B. A. (2011) The magnetic properties of Quaternary aeolian dusts and sediments, and their palaeoclimatic

893   significance. *Aeolian Res.* **3**, 87–144.

894   Maher B. A., Karloukovski V. and Mutch T. (2004) High-field remanence properties of synthetic and natural

895   submicrometre haematites and goethites: significance for environmental contexts. *Earth Planet. Sci. Lett.* **226**,

896   491–505.

897   Maher B. A. and Taylor R. M. (1988) Formation of ultrafine-grained magnetite in soils. *Nature* **336**, 368.

898   Maher B. A. and Thompson R. (1992) Paleoclimatic Significance of the Mineral Magnetic Record of the Chinese

899   Loess and Paleosols. *Quat. Res.* **170**, 155–170.

900   Manceau A., Tamura N., Marcus M. A., MacDowell A. A., Celestre R. S., Sublett R. E., Sposito G. and Padmore H.

901   A. (2002) Deciphering Ni sequestration in soil ferromanganese nodules by combining X-ray fluorescene,

902   absorption, and diffraction at micrometer scales of resolution. *Am. Mineral.* **87**, 1494–1499.

903   Manning A. H., Ball L. B., Wanty R. B. and Williams K. H. (2020) Direct observation of the depth of active

904   groundwater circulation in an alpine watershed. *Water Resour. Res.* **57**, WR028548.

905   Manning A. H., Verplanck P. L., Caine J. S. and Todd A. S. (2013) Links between climate change, water-table

906   depth, and water chemistry in a mineralized mountain watershed. *Appl. Geochemistry* **37**, 64–78.

907   Marcus M. A., MacDowell A. A., Celestre R., Manceau A., Miller T., Padmore H. A. and Sublett R. E. (2004)

908   Beamline 10.3.2 at ALS: A hard X-ray microprobe for environmental and materials sciences. *J. Synchrotron*

909   *Radiat.* **11**, 239–247.

910   Mast M. A., Turk J. T., Clow D. W. and Campbell D. H. (2011) Response of lake chemistry to changes in

911   atmospheric deposition and climate in three high-elevation wilderness areas of Colorado. *Biogeochemistry*

912   **103**, 27–43.

913   Maxbauer D. P., Feinberg J. M. and Fox D. (2016) MAX UnMix: A web application for unmixing magnetic

914   coercivity distributions. *Comput. Geosci.* **95**, 140–145.

915   Meybeck M. (1987) Global chemical weathering of surficial rocks estimated from river dissolved loads. *Am. J. Sci.*

916   **287**, 401–428.

917   Moncur M. C., Jambor J. L., Ptacek C. J. and Blowes D. W. (2009) Mine drainage from the weathering of sulfide

918   minerals and magnetite. *Appl. Geochemistry* **24**, 2362–2373.

919   Moore D. M. and Reynolds R. C. (1997) *X-ray diffraction and identification and analysis of clay minerals*. Oxford

920   Uni., New York.

921   Morin F. (1950) Magnetic susceptibility of αFe2O3 and αFe2O3 with added titanium. *Phys. Rev.* **78**, 819–820.

922   Muñoz M., De Andrade V., Vidal O., Lewin E., Pascarelli S. and Susini J. (2006) Redox and speciation

923   micromapping using dispersive X-ray absorption spectroscopy: Application to iron in chlorite mineral of a

924   metamorphic rock thin section. *Geochemistry, Geophys. Geosystems* **7**, Q11020.

925   Nordstrom D. K. (2011) Hydrogeochemical processes governing the origin, transport and fate of major and trace

926   elements from mine wastes and mineralized rock to surface waters. *Appl. Geochemistry* **26**, 1777–1791.

927 Ozdemir O. and Dunlop D. J. (2010) Hallmarks of maghemitization in low-temperature remanence cycling of

928   partially oxidized magnetite nanoparticles. *J. Geophys. Res. Earth Surf.* **115**, B02101.

929 Pannalal S. J., Crowe S. A., Cioppa M. T., Symons D. T., Sturm A. and Fowle D. A. (2005) Room-temperature

930   magnetic properties of ferrihydrite: A potential magnetic remanence carrier? *Earth Planet. Sci. Lett.* **236**, 856–

931   870.

932 Parviainen A., Cruz-Hernández P., Pérez-López R., Nieto J. M. and Delgado-López J. M. (2015) Raman

933   identification of Fe precipitates and evaluation of As fate during phase transformation in Tinto and Odiel

934   River Basins. *Chem. Geol.* **398**, 22–31.

935 Peak D. and Sparks D. L. (2002) Mechanisms of selenate adsorption on iron oxides and hydroxides. *Environ. Sci.*

936   *Technol.* **36**, 1460–1466.

937 Peter C. and Dekkers M. (2003) Selected room temperature magnetic parameters as a function of mineralogy,

938   concentration and grain size. *Phys. Chem. Earth, Parts A/B/C* **28**, 659–667.

939 Post J. E. (1999) Manganese oxide minerals: Crystal structures and economic and environmental significance. *Proc.*

940   *Natl. Acad. Sci. U. S. A.* **96**, 3447–3454.

941 Potter D. and Stephenson A. (1986) The detection of fine particles of magnetite using anhysteretic and rotational

942   remanent magnetizations,. *GeoJI* **87**, 569–582.

943 Putz H. and Brandenburg K. (2011) Match! - Phase identification from powder diffraction, cristal impact. , 137.

944 Ravel B. and Newville M. (2005) ATHENA, ARTEMIS, HEPHAESTUS: data analysis for X-ray absorption

945   spectroscopy using IFEFFIT. *J. Synchrotron Radiat.* **12**, 537–41.

946 Rochette P., Fillion G., Mattie J.-L. and Dekkers M. (1990) Magnetic transition at 30-34 Kelvin in pyrrhotite:

947   Insight into a widespread occurrence of this mineral in rocks. *Earth Planet. Sci. Lett.* **98**, 319–328.

948 Rosera J. M., Gaynor S. P. and Coleman D. S. (2021) Spatio-temporal shifts in magmatism and mineralization in

949   Northern Colorado beginning in the late eocene. *Econ. Geol.* **116**, 987–1010.

950 Seedorff E., Diller J. h, Proffett J. M. J., Einaudi M. T., Zurcher L., Stavast W. J. A., Johnson D. A. and Barton M.

951   D. (2005) Porphyric deposits: characteristics amd origin of hypogene feature. *Econ. Geol.* **100**, 251–298.

952 Sharp J. E. (1978) A molybdenum mineralized breccia pipe complex, Redwell Basin, Colorado. *Econ. Geol.* **73**,

953   369–382.

954   Sherman D. M. and Randall S. R. (2003) Surface complexation of arsenic(V) to iron(III) (hydr)oxides: Structural

955   mechanism from ab initio molecular geometries and EXAFS spectroscopy. *Geochim. Cosmochim. Acta* **67**,

956   4223–4230.

957   Slotznick S. P., Swanson-Hysell N. L. and Sperling E. A. (2018) Oxygenated Mesoproterozoic lake revealed

958   through magnetic mineralogy. *Proc. Natl. Acad. Sci. U. S. A.* **115**, 12938–12943.

959   Slotznick S. P., Webb S. M., Kirschvink J. L. and Fischer W. W. (2019) Mid-Proterozoic ferruginous conditions

960   reflect postdepositional processes. *Geophys. Res. Lett.* **46**, 3114–3123.

961   Snowball I. F. (1997) The detection of single-domain greigite (Fe3S4) using rotational remanent magnetization

962   (RRM) and the effective gyro field (Bg): mineral magnetic and palaeomagnetic applications. *GeoJI* **130**, 703–

963   716.

964   Sullivan P. L., Goddéris Y., Shi Y., Gu X., Schott J., Hasenmueller E. A., Kaye J., Duffy C., Jin L. and Brantley S.

965   L. (2019) Exploring the effect of aspect to inform future earthcasts of climate-driven changes in weathering of

966   shale. *J. Geophys. Res. Earth Surf.* **124**, 974–993.

967   Sullivan P. L., Hynek S. A., Gu X., Singha K., White T., West N., Kim H., Clarke B., Kirby E., Duffy C. and

968   Brantley S. L. (2016) Oxidative dissolution under the channel leads geomorphological evolution at the shale

969   hills catchment. *Am. J. Sci.* **316**, 981–1026.

970   Suzuki Y., Kopp R. E., Kogure T., Suga A., Takai K., Tsuchida S., Ozaki N., Endo K., Hashimoto J. and Kato Y.

971   (2006) Sclerite formation in the hydrothermal-vent "scaly-foot" gastropod—possible control of iron sulfide

972   biomineralization by the animal. *Earth Planet. Sci. Lett.* **242**, 39–50.

973   Swanson-Hysell N. L., Maloof A. C., Kirschvink J. L., Evans D. A. D., Halverson G. P. and Hurtgen M. T. (2012)

974   Constraints on neoproterozoic paleogeography and paleozoic orogenesis from paleomagnetic records of the

975   bitter springs formation, amadeus basin, central Australia. *Am. J. Sci.* **312**, 817–884.

976   Taylor K. G. and Macquaker J. . H. S. (2014) Diagenetic alterations in a silt- and clay-rich mudstone succession: an

977   example from the Upper Cretaceous Mancos Shale of Utah, USA. *Clay Miner.* **49**, 213–227.

978   Thomas J. A. and Galey J. T. (1982) Exploration and geology of the Mt. Emmons molybdenite deposits, Gunnison

979   County, Colorado. *Econ. Geol.* **77**, 1085–1104.

980   Thomson G. F. (1990) The anomalous demagnetization of pyrrhotite. *GeoJI* **103**, 425–430.

981   Toner B. M., Rouxel O. J., Santelli C. M., Bach W. and Edwards K. J. (2016) Iron transformation pathways and

982   redox micro-environments in seafloor sulfide-mineral deposits: Spatially resolved Fe XAS and δ57/54Fe

983   observations. *Front. Microbiol.* **7**, 648.

984 Tuttle M. L. W., Fahy J. W., Elliott J. G., Grauch R. I. and Stillings L. L. (2014) Contaminants from Cretaceous

985   black shale: I. Natural weathering processes controlling contaminant cycling in Mancos Shale, southwestern

986   United States, with emphasis on salinity and selenium. *Appl. Geochemistry* **46**, 57–71.

987 Tweto O. and Sims P. K. (1963) Precambrian ancestry of the Colorado Mineral Belt. *GSA Bull.* **78**, 991–1014.

988 Verplanck P. L., Nordstrom D. K., Bove D. J., Plumlee G. S. and Runkel R. L. (2009) Naturally acidic surface and

989   ground waters draining porphyry-related mineralized areas of the Southern Rocky Mountains, Colorado and

990   New Mexico. *Appl. Geochemistry* **24**, 255–267.

991 Verplanck P. L., Wanty R. B., Berger B. R., Tuttle M. L., Kimball B. A. and Farmer G. L. (2004)

992   Hydrogeochemistry of an acidic, alpine watershed, Redwell Basin, Colorado. *Proc. - Int. Symp. Water-Rock*

993   *Interact.* **11**, 1649–1653.

994 Verwey E. (1939) Electronic conduction of magnetite (Fe3O4) and its transition point at low temperatures. *Nature*

995   **144**, 327–328.

996 Wanty R. B., Verplanck P. L., Tuttle M. L., Runkel R. L., Berger B. R. and Kimball B. A. (2004) Resolving natural

997   and anthropogenic sources of solutes to a watershed from historic mining. *Proc. - Int. Symp. Water-Rock*

998   *Interact.* **11**, 1659–1663.

999 Waychunas G. A., Kim C. S. and Banfield J. F. (2005) Nanoparticulate iron oxide minerals in soils and sediments:

1000   Unique properties and contaminant scavenging mechanisms. *J. Nanoparticle Res.* **7**, 409–433.

1001 Webb S. M. (2011) The Microanalysis toolkit: X-ray fluorescence image processing software. In *AIP Conference*

1002   *Proceedings* pp. 196–199.

1003 West A. J., Galy A. and Bickle M. (2005) Tectonic and climatic controls on silicate weathering. *Earth Planet. Sci.*

1004   *Lett.* **235**, 211–228.

1005 Williams A. G. B. and Scherer M. M. (2004) Spectroscopic evidence for Fe(II)-Fe(III) electron transfer at the iron

1006   oxide-water interface. *Environ. Sci. Technol.* **38**, 4782–4790.

1007

List of figures

1009   **Figure 1.** Geographic location of Redwell Basin in Colorado, USA. Geological and topographical
1010 map of the basin (Gaskill et al., 1967) showing location of the MW1 drill site, the Red Well spring,
1011 Redwell Creek, Mt. Emmons Porphyry deposit, and the Daisy Mine. Satellite image (Google Earth)
1012 showing the boundary of Redwell Basin.

1013   **Figure 2.** Photographs and bulk mineral and elemental analyses of the Redwell Basin core MW1. **(a)**
1014 Bulk mineralogy of the MW1 core from bulk X-ray diffraction with photographs of select sample
1015 locations at selected depth. The coin shown is 1 inch in diameter. Rocks sampled at each depth can be
1016 seen in more detail in **Figure S2.** Black circles with central "X" marks indicate the sampled location. **(b)**
1017 Bulk analysis of major elements (normalized using the mass transfer coefficient, τ_{Zn}, with Zr as immobile
1018 element) and a white sandstone sample collected at 12.1 m bgs (as the least altered unweathered reference
1019 sample) and trace elements. Star symbol marks the depth at which a fracture-surface sample was analyzed
1020 using room- and low-temperature magnetic methods and microscale X-ray fluorescence
1021 spectromicroscopy. Circle symbols mark depths at which background samples were analyzed by with
1022 room- and low-temperature magnetic methods. Triangle symbol marks depths at which additional
1023 fracture-surface samples were only analyzed with room-temperature magnetic methods. No symbols are
1024 included for the additional background samples only analyzed magnetically at room-temperature.

1025   **Figure 3.** Magnetic analysis of ferromagnetic minerals (*sensu lato*) in samples from the MW1 drill
1026 core **(a)** Low-temperature magnetic experiments from unweathered samples in the MW1 drill core at
1027 depths of 3.3, 3.9, 5.1 and 27.3 m bgs. Sample denoted 3.3-BOT is a ~2-mm thick rock slice from
1028 unweathered region of the fracture surface at 3.3 m bgs. Abbreviations: LTSIRM = low-temperature
1029 saturation isothermal remanent magnetization, FC = field cooled, ZFC = zero-field cooled, RTSIRM =
1030 room-temperature saturation isothermal remanent magnetization, SP = superparamagnetic minerals. **(b)**
1031 Relative proportions of magnetic mineral components in samples from the MW1 drill core based on
1032 fitting of IRM demagnetization coercivity spectra (**Fig. S5**). Ranges of coercivity values are consistent
1033 with minerals shown to be present through low-temperature magnetic methods. High coercivity (range of
1034 139 to 527 mT, red) could be attributed to hematite and/or goethite; high-moderate coercivity (range 41 to
1035 111 mT, yellow) is attributed to pyrrhotite; and moderate coercivity (range 12 to 31 mT, blue) is
1036 attributed to magnetite. The low coercivity component (range 5 to 7 mT, cyan) could be magnetite of a
1037 distinct grain size, titanomagnetite, unknown sulfide mineral, or coarse ferrihydrite. In the right plot, the
1038 saturation magnetism (M_s) in blue and the fraction of paramagnetic minerals in green (ratio of high-field
1039 to low-field susceptibility) obtained from hysteresis loops are shown.

1040   **Figure 4. a)** Photograph of the Mesaverde Formation drill core MW1 at a depth of 3.3 m bgs (left)

1041   and a cross-section of the core at the weathered fracture surface (right). The labels STOP, TOP, MID and

1042   BOTTOM refer to rock-chip samples cut from the same block for magnetism measurements. The purple

1043   square in the weathering profile indicates the area where μXRF mapping. The location of display SEM

1044   images (black dots) were ordered according to their position with respect to the fracture surface, from the

1045   shallowest (I) to the deepest (VII). **b)** Back-scattered electron (BSE) images from (**b-I**) the Fe-rich

1046   coating at the fracture surface where the layered banding is observed. Images below show a detailed a

1047   high magnification selected location demarked by a yellow box in the weathering profile with its O

1048   distribution map. (**c-II**) Intermixed lead and iron (oxyhydr)oxides (Pb- and Fe-Oxy) in the weathering

1049   region inferred to be the product of in-situ oxidation of metal sulfide minerals. (**c-III**) Plagioclase (Pl)

1050   grain, close to the fracture surface with irregular morphology consistent with hydrothermal alteration,

1051   associated with sericite (Ser) and iron (oxyhydr)oxide precipitation. (**c-IV**) Non-weathered region

1052   showing evidence of pyrrhotite (Po) and sphalerite (Sp) co-precipitation with siderite (Sd) during

1053   hydrothermal alteration. (**c-V**) Intermixed siderite and Mn-rich calcite (Mn-Cal) in the weathered region.

1054   (**c-VI**) Siderite, sphalerite and galena (Gn) precipitated from hydrothermal fluids in the non-weathered

1055   region. Feldspar (Fsp) grains in the same region display pervasive hydrothermal alteration. (**c-VII**)

1056   Chlorite (Chl) from hydrothermal fluids in the non-weathered region and kaolinite (Kln). Black areas in

1057   BSE images **b-I**, **c-II**, and **c-III** correspond to empty space (pores), which are not observed in other

1058   sample locations. Mineral identification is based upon energy-dispersive X-ray spectroscopy (EDX) data.

1059   Multi-element EDX maps from BSE images in b) and c) are shown in **Figure S7 and S8**.

1060   **Figure 5.** Synchrotron μXRF maps (**a**) and integrated elemental profiles (**b**) of major and trace

1061   elements in the fracture weathering profile from MW1 core at 3.3 m bgs. The data reveal weathering

1062   profiles in Ca and Mn (top) and S, Zn and other elements (bottom). Red triangle indicates the fracture

1063   surface location, the blue triangle indicates the carbonate minerals and chlorite weathering front and green

1064   triangle the sulfide minerals weathering front. Selenium map was recorded at 13000 eV (above the Se K-

1065   edge). The Zn map was collected at 10000 eV (above the Zn K-edge). The Fe, Mn, Ca, K maps were

1066   recorded at 7210 eV (above the Fe K-edge). These maps were recorded at SSRL 2-3. White rectangles

1067   indicate the Fe chemical mapping region. The Si, Al and S maps were recorded at 2522 eV (above the S

1068   K-edge) at ALS XFM 10.3.2. The elemental profiles are the horizontal integrations of the two-

1069   dimensional maps. The vertical dashed lines indicate the elemental average concentration above or below

1070   the oxidative weathering front (green arrows) for Fe, Mn, Ca, Si, Al, K, S, Se and Zn. The] symbol

1071   highlights the ~0.5-mm band of elevated iron and other elements inferred to represent weathering at a

1072   microfracture open to groundwater.

1073   **Figure 6**. **a)** μXRF distribution maps of Fe(II) and Fe (III) in the fracture weathering profile from

1074   MW1 core at 3.3 m bgs were obtained by multi-energy mapping at SSRL beamline 2-3 (see methods

1075   section). Solid red triangle indicates the fracture surface location, the blue triangle indicates the carbonate

1076   minerals and chlorite weathering front and green triangle the sulfide minerals weathering front. Numbered

1077   locations indicated by same geometric symbols (open triangle, circle, square or diamond) gave similar Fe

1078   K-edge μXANES spectra. **b)** Fe K-edge μXANES spectra on representative spots along with best least-

1079   square linear combination fits (LCF), best matching goethite, chlorite, biotite and siderite. All spectra can

1080   be found in **Fig. S9**.

1081   **Figure 7. a)** μXRF distribution maps of sulfur in the fracture weathering profile from MW1 core at

1082   3.3 m bgs recorded at 2700 eV (above the S K-edge) from ALS beamline 10.3.2. Red triangle indicates

1083   the fracture surface location, the blue triangle indicates the carbonate minerals and chlorite weathering

1084   front and green triangle the sulfide minerals weathering front. Numbered locations indicated by same

1085   geometric symbol (star and hexagon) gave similar S K-edge μXANES spectra. **b)** Sulfur K-edge

1086   μXANES spectra obtained at selected numbered locations compared to bulk references from standards

1087   database. All spectra can be found in **Fig. S9**.

1088   **Figure 8.** Magnetic analysis of ferromagnetic minerals (*sensu lato*) in thin rock slices from three

1089   weathered fracture surfaces. **(a)** Low-temperature magnetic measurements on four rock slices cut from the

1090   weathered fracture surface at 3.3 m bgs. The slice locations are labeled in **Fig. 4.** BOT is the bottommost

1091   (unweathered, > 10 mm from the fracture surface) slice from the series and STOP is the fracture surface.

1092   The abbreviations of the measurement techniques are given in **Fig. 3** caption. **(b)** Relative proportions of

1093   magnetic mineral components based on fitting of IRM demagnetization coercivity spectra (**Fig. S11 and**

1094   **S12**). The interpretation of the ranges in coercivity values are given in **Fig. 3** caption.

1095   **Figure 9.** Conceptual model of the fracture-scale weathering profile observed in mineralized

1096   Mesaverde Formation sandstone, showing the principal weathering fronts, element transport within the

1097   rock and retention or release into groundwater. Red triangle indicates the rock-groundwater interface at

1098   the fracture, the blue triangle indicates the chlorite and carbonate mineral weathering front, and the green

1099   triangle indicates the sulfide mineral weathering front. Minerals that dissolve (e.g., sphalerite) or that

1100   precipitate (e.g., jarosite) during weathering are written in normal and italic text, respectively. Zinc

1101   cations are partly retained, likely by adsorption to goethite. Quartz is distributed throughout the rock and

1102   are negligibly dissolved during weathering. Feldspar (Albite and K-Feldspar) and chlorite are partially

1103   dissolved during weathering, whereas muscovite and illite (i.e., sericite) increase their abundant toward de

1104   fracture surface. *Pyrite is included in the conceptual model as one of the main sources of Fe in this

1105   system, even though it was not detected at the 3.3 m MW1 weathering profile. Abbreviations: Zn(ad) =
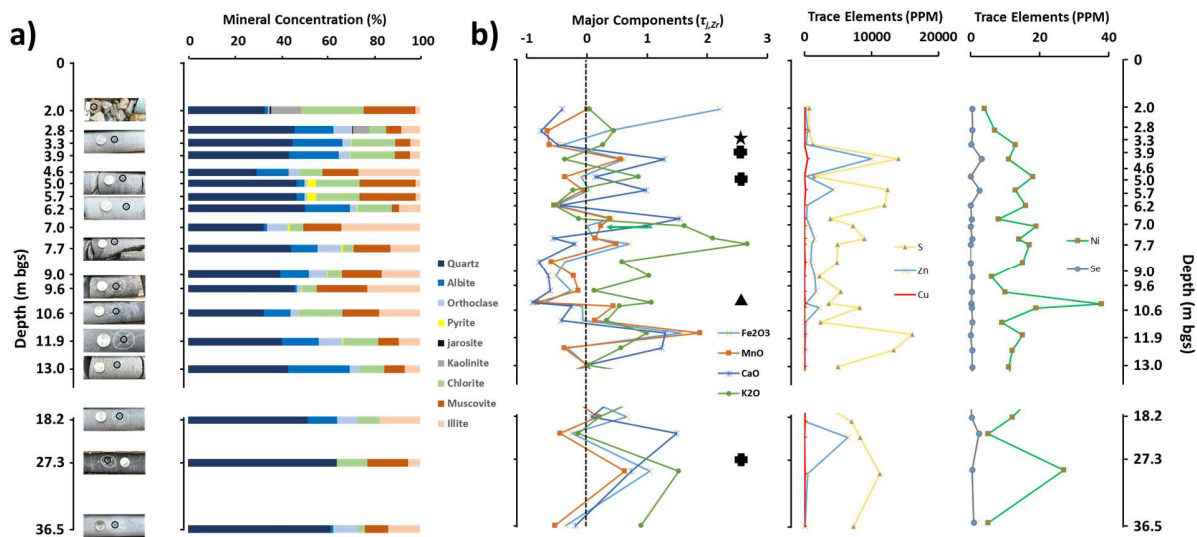
1106   adsorbed zinc.

1107   Figure 1
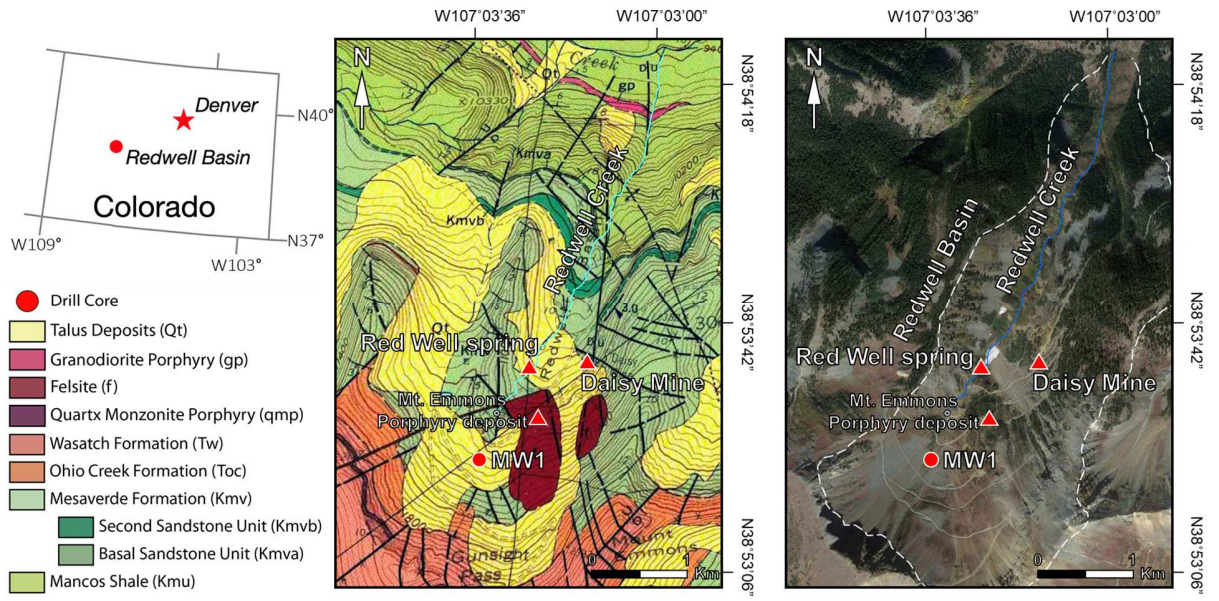
1108
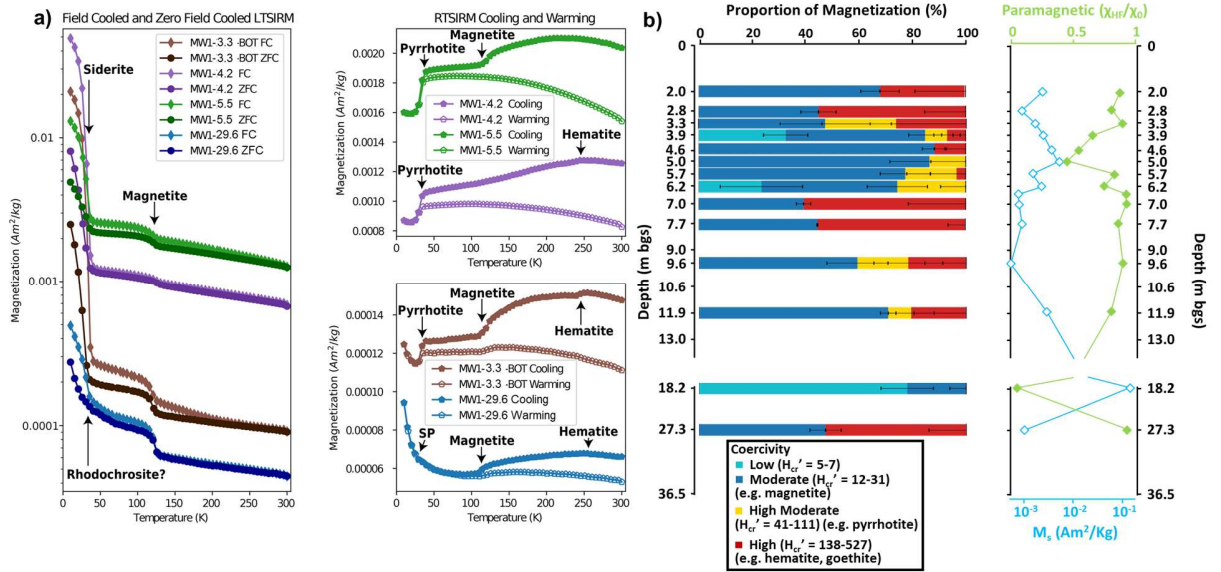
1109

1110   Figure 2

1111
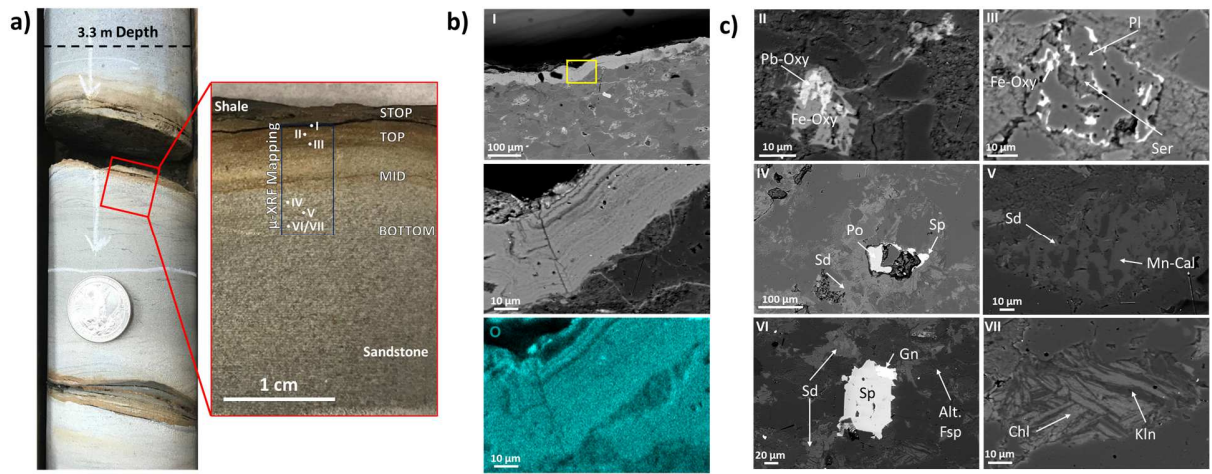
1112

1113   Figure 3

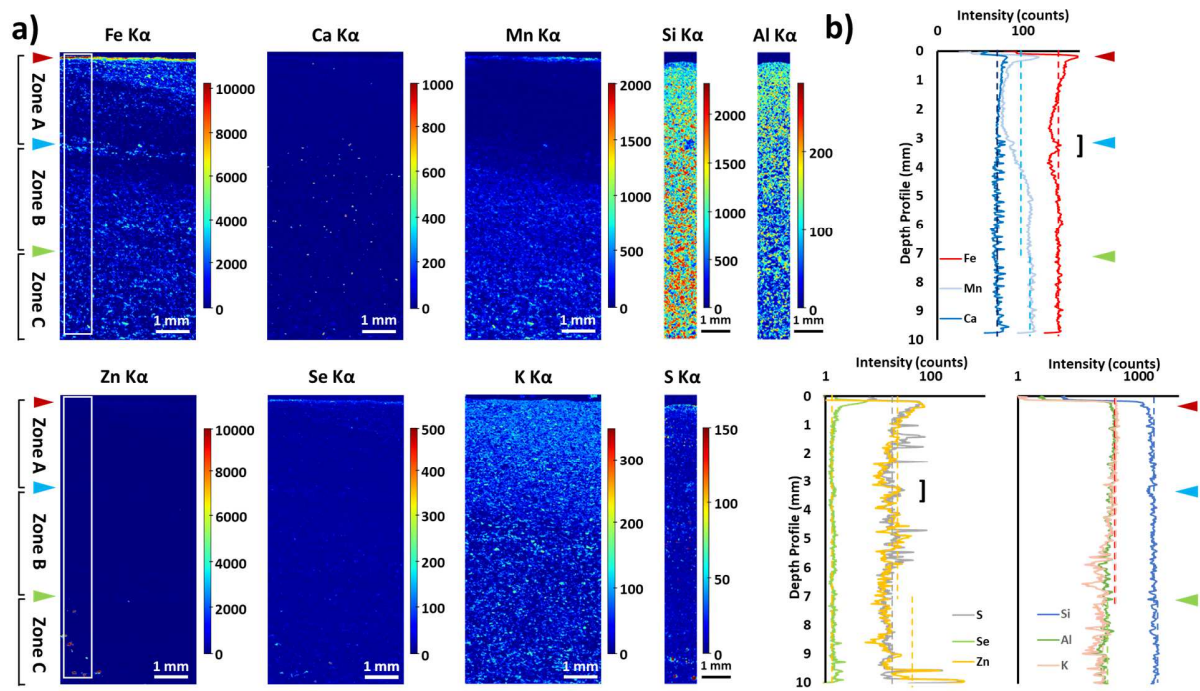1114

1115

1116   Figure 4

1117

1118

1119   Figure 5
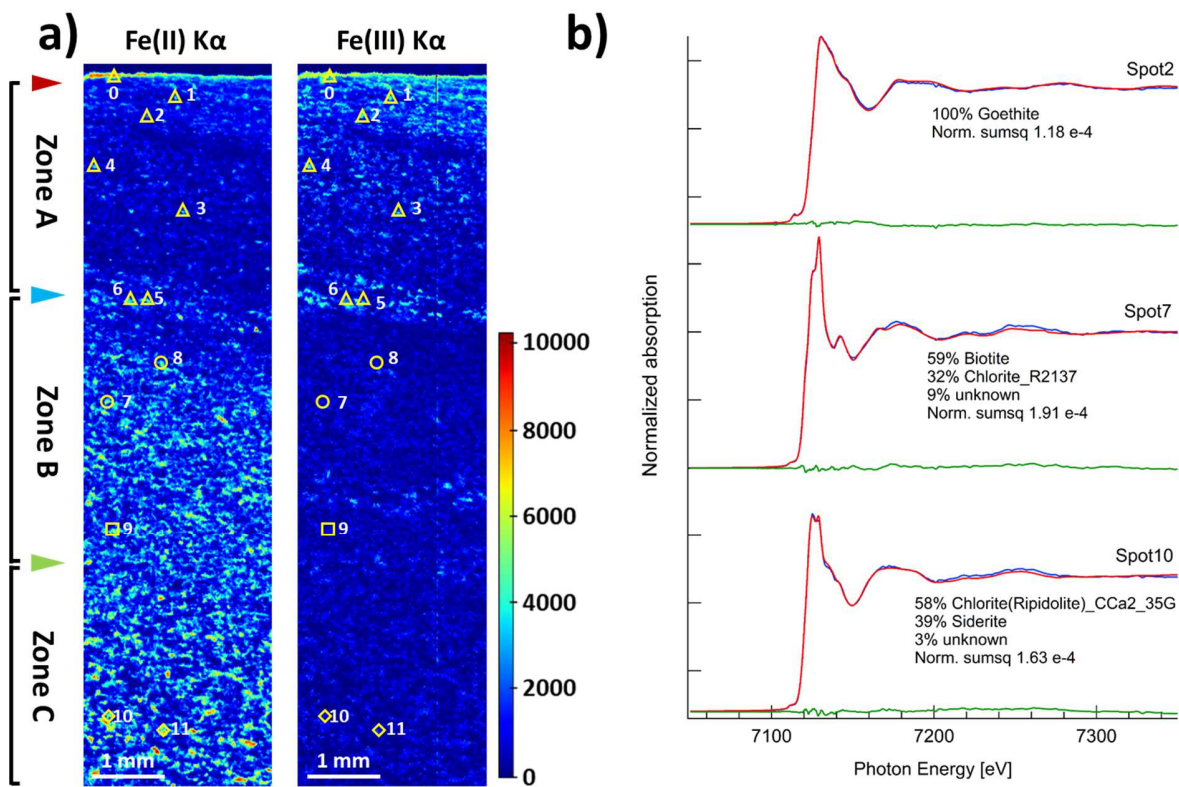

1120

1121

1122   Figure 6

1123

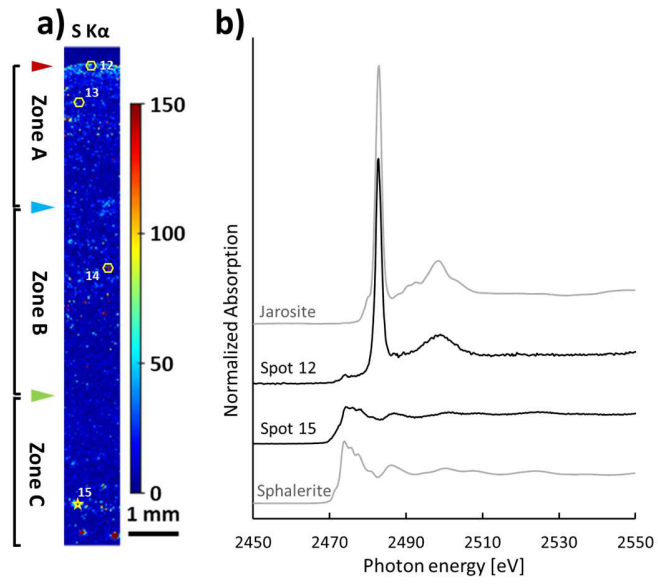1124

1125   Figure 7
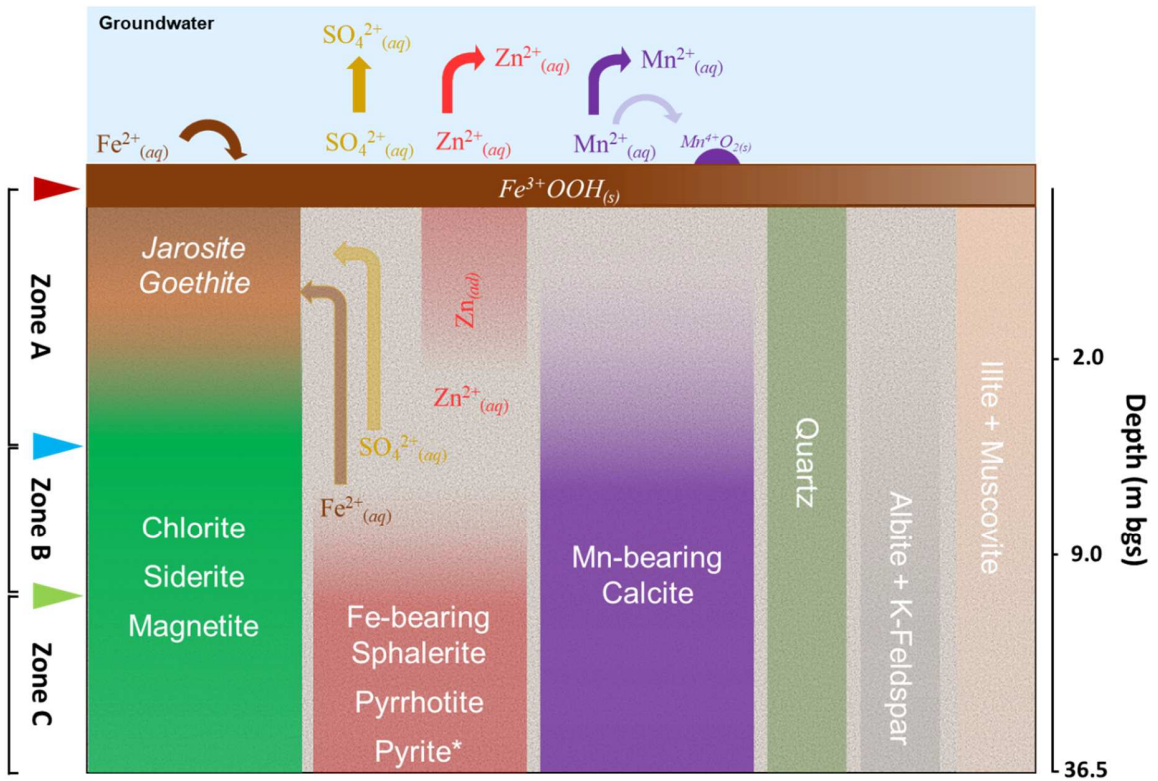

1126

1127

1128   Figure 8

1129

1130

1131   Figure 9

1132